remote sensing

MDPI

Article

Lithological and Hydrothermal Alteration Mapping of Epithermal, Porphyry and Tourmaline Breccia Districts in the Argentine Andes Using ASTER Imagery

Francisco J. Testa [1,2,*], Cecilia Villanueva [3,4], David R. Cooke [1,2] and Lejun Zhang [1,2]

1 CODES, Centre for Ore Deposit and Earth Sciences, University of Tasmania, Private Bag 79, Hobart, Tasmania 7001, Australia; D.Cooke@utas.edu.au (D.R.C.); Lejun.Zhang@utas.edu.au (L.Z.)
2 Transforming the Mining Value Chain, an ARC Industrial Transformation Research Hub, University of Tasmania, Private Bag 79, Hobart, Tasmania 7001, Australia
3 School of Land and Food, Geography and Spatial Science, University of Tasmania, Private Bag 78, Hobart, Tasmania 7001, Australia; Cecilia.Villanueva@utas.edu.au
4 Institute for Marine and Antarctic Studies, University of Tasmania, Private Bag 49, Hobart, Tasmania 7001, Australia
* Correspondence: F.J.Testa@utas.edu.au

Received: 15 October 2017; Accepted: 15 January 2018; Published: 30 January 2018

Abstract: The area of interest is located on the eastern flank of the Andean Cordillera, San Juan province, Argentina. The 3600 km^2 area is characterized by Siluro-Devonian to Neogene sedimentary and igneous rocks and unconsolidated Quaternary sediments. Epithermal, porphyry-related, and magmatic-hydrothermal breccia-hosted ore deposits, common in this part of the Frontal Cordillera, are associated with various types of hydrothermal alteration assemblages. Kaolinite – alunite-rich argillic, quartz – illite-rich phyllic, epidote – chlorite – calcite-rich propylitic and silicic are the most common hydrothermal alteration assemblages in the study area. VNIR, SWIR and TIR ASTER data were used to characterize geological features on a portion of the Frontal Cordillera. Red-green-blue band combinations, band ratios, logical operations, mineral indices and principal component analysis were applied to successfully identify rock types and hydrothermal alteration zones in the study area. These techniques were used to enhance geological features to contrast different lithologies and zones with high concentrations of argillic, phyllic, propylitic alteration mineral assemblages and silicic altered rocks. Alteration minerals detected with portable short-wave infrared spectrometry in hand specimens confirmed the capability of ASTER to identify hydrothermal alteration assemblages. The results from field control areas confirmed the presence of those minerals in the areas classified by ASTER processing techniques and allowed mapping the same mineralogy where pixels had similar information. The current study proved ASTER processing techniques to be valuable mapping tools for geological reconnaissance of a large area of the Argentinean Frontal Cordillera, providing preliminary lithologic and hydrothermal alteration maps that are accurate as well as cost and time effective.

Keywords: ASTER; geology; hydrothermal alteration; mineralization; epithermal; porphyry; magmatic-hydrothermal breccia pipe

1. Introduction

Base and precious metals cannot be detected by remote sensing but the widely developed hydrothermal alteration minerals associated with some ore deposits can. Certain diagnostic group of hydrothermal minerals, such as clays, phyllosilicates, sulfates and carbonates, can be identified based on their spectral signatures, with diagnostic features mainly in the shortwave infrared (SWIR) portion

of the electromagnetic spectrum [1–4]. Iron oxides and hydroxides normally have lower reflectance in the visible region and higher reflectance in the near infrared wavelengths, making the visible and near infrared (VNIR) portion of the spectrum critical for the study of these minerals [1,5].

Lithology and mineral mapping using satellite imagery has been conducted successfully since the first Landsat satellite was launched in 1972. More recently, Landsat-8 was launched in February 2013 with two instruments: the reflective band Operational Land Imager (OLI) sensor and the Thermal Infrared Sensor (TIRS) [6]. Although Landsat TM/ETM+ and Landsat OLI/TIRS have the capability of detecting ferric oxides and hydroxides, OH-bearing minerals and carbonate-rich alteration zones, they cannot identify specific minerals. Bands 1–4 (Landsat ETM+) and 1–5 (Landsat OLI) record energy from the VNIR portion of the electromagnetic spectrum where hematite, goethite and jarosite's diagnostic features occur (Figure 1; Table 1). Bands 5 and 7 (Landsat ETM+) and 9, 6, 7 (Landsat OLI) have the capability of recording information from the SWIR range (Figure 1; Table 1) where minerals like alunite, kaolinite, dickite, pyrophyllite, zunyite, montmorillonite, illite, muscovite, chlorite, epidote and calcite exhibit their diagnostic features [7–9]. Bands 6 (Landsat ETM+) and 10–11 (Landsat TIRS) cover the thermal infrared (TIR) portion of the electromagnetic spectrum (Figure 1; Table 1).

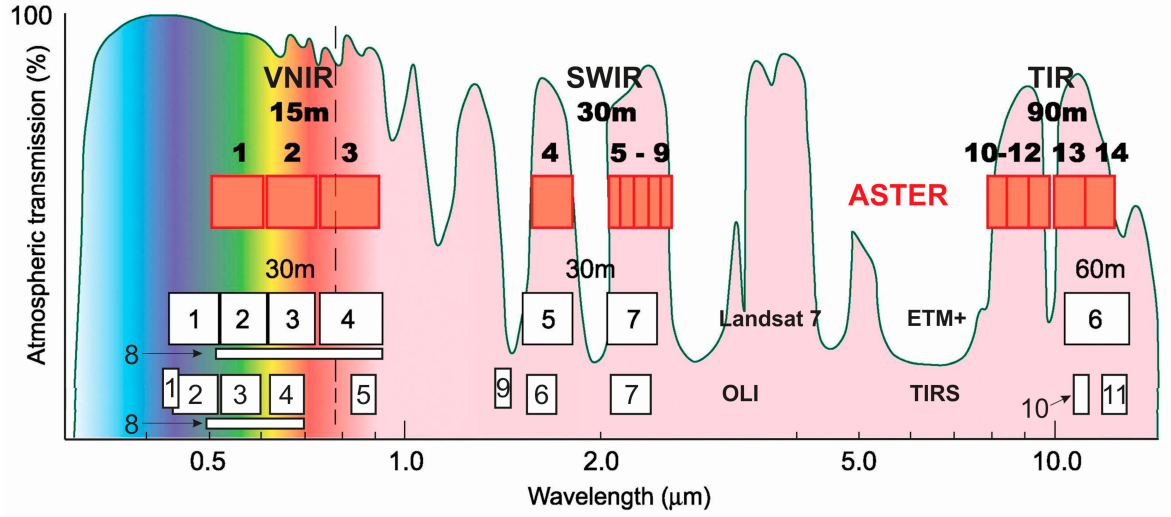

Figure 1. Electromagnetic spectrum comparing ASTER and Landsat (ETM+ and OLI/TIRS) bands. The spatial resolution for bands in the visible and near infrared (VNIR), short-wave infrared (SWIR) and thermal infrared (TIR) are specified for each sensor. The vertical dashed line represents the end of the visible light. Figure based on [9–13].

The Advanced Spaceborne Thermal Emission and Reflection Radiometer (ASTER) is a sensor on-board the EOS/Terra platform launched by NASA in 1999. ASTER consists of three separate instrument subsystems, each of which operates in a different spectral region. Bands 1–3, 4–9 and 10–14 cover the VNIR, SWIR and TIR portion of the electromagnetic spectrum respectively (Figure 1; Table 1). The spatial resolution varies depending on the subsystem: VNIR has a resolution of 15 m, SWIR 30 m and TIR 90 m [14–19]. It is the first multispectral spaceborne sensor able to discriminate OH-bearing minerals given the larger number of bands within the SWIR region [14].

Table 1. Comparative table that highlights number of spectral bands and their characteristic features (i.e., wavelength and spatial resolution) in ASTER, Landsat-7 (ETM+) and Landsat-8 (OLI/TIRS).

ASTER			Landsat-7 (ETM+)			Landsat-8 (OLI/TIRS)		
Bands	**Wavelength (μm)**	**Res. (m)**	**Bands**	**Wavelength (μm)**	**Res. (m)**	**Bands**	**Wavelength (μm)**	**Res. (m)**
						1—Ultra blue (coastal/aerosol)	0.435–0.451	30
			1—Visible blue	0.45–0.52	30	2—Visible blue	0.452–0.512	30
1—Visible green/yellow	0.520–0.600	15	2—Visible green	0.52–0.60	30	3—Visible green	0.533–0.590	30
2—Visible red	0.630–0.690	15	3—Visible red	0.63–0.69	30	4—Visible red	0.636–0.673	30
3N—NIR	0.760–0.860	15	4—NIR	0.77–0.90	30	5—NIR	0.851–0.879	30
3B—NIR	0.760–0.860	15						
			8—Panchromatic	0.52–0.90	15	8—Panchromatic	0.503–0.676	15
						9—Cirrus	1.363–1.384	30
4—SWIR	1.600–1.700	30	5—SWIR	1.55–1.75	30	6—SWIR	1.566–1.651	30
5—SWIR	2.145–2.185	30	7—SWIR	2.09–2.35	30	7—SWIR	2.107–2.294	30
6—SWIR	2.185–2.225	30						
7—SWIR	2.235–2.285	30						
8—SWIR	2.295–2.365	30						
9—SWIR	2.360–2.430	30						
10—TIR	8.125–8.475	90						
11—TIR	8.475–8.825	90						
12—TIR	8.925–9.275	90						
13—TIR	10.250–10.950	90	6—TIR	10.40–12.50	(30)	10—TIR	10.60–11.19	(30)
14—TIR	10.950–11.650	90				11—TIR	11.50–12.51	(30)

Res. = Resolution; (30) = Landsat-7 ETM+ Band 6 is acquired at 60 m resolution but is resampled to 30 m pixels; Landsat-8 TIRS bands are acquired at 100 m resolution but are resampled to 30 m pixels.

We have undertaken detailed image processing of an ASTER scene from north-western San Juan province, Argentina, which covers part of the eastern flank of the Frontal Cordillera (Figure 2). This geological province, on the eastern side of the Andean Cordillera, extends from northern La Rioja to southern Mendoza provinces. The scene covers a 3600 km^2 area between latitude 30°29′22.49′′S and 31°8′47.37′′S, and longitude 69°15′9.01′′W and 70°3′58.69′′W. A portion of the study area, close to the Castaño River, was previously studied from a remote sensing perspective. The hydrothermal alteration was characterized by applying principal component analysis (PCA) to Landsat TM imagery [20]. In this article, we are expanding the hydrothermal alteration characterization and providing lithologic mapping of a larger area using ASTER imagery. ASTER has three times more SWIR bands and five times more TIR bands than Landsat-7 (ETM+), enhancing the capability for specific mineral detection and lithologic characterization (Figure 1; Table 1). Figure 1 and Table 1 compare the number of bands, their bandwidths and locations within the electromagnetic spectrum for ASTER, Landsat-7 (ETM+) and Landsat-8 (OLI/TIRS).

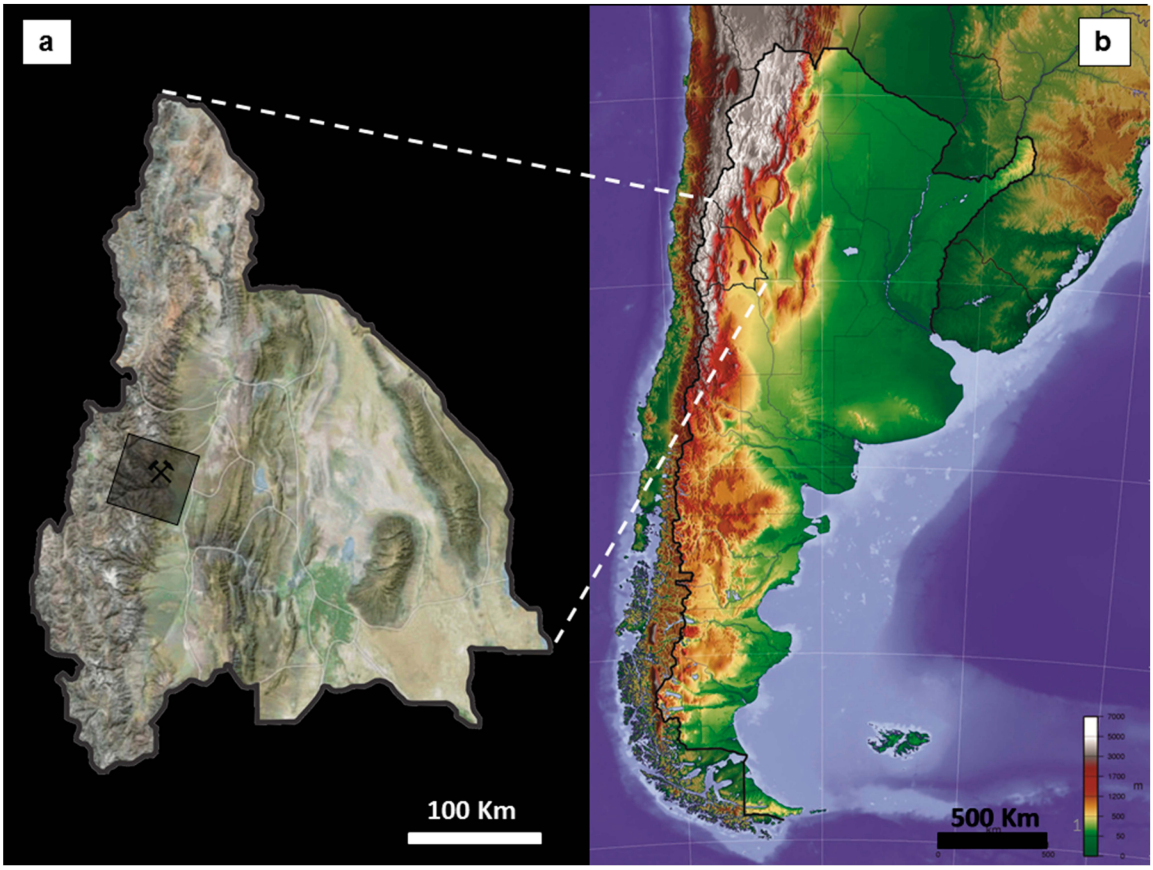

Figure 2. Map of San Juan province (**a**) and Argentina (**b**). The shaded square in Figure 2a represents the area of the ASTER scene used for the current study. The crossed hammers symbol indicates the location of the San Francisco de los Andes mine.

The aim of this study is to utilize the entire ASTER scene (scale 1:400,000) to map the spatial distribution of different types of lithologic units, hydrothermal alteration assemblages and individual minerals on an area of the eastern flank of the Argentinean Frontal Cordillera, with various epithermal, porphyry and breccia-hosted deposits [21]. We intend to improve and provide further lithologic information to that presented in the geologic map drawn for this study (based only on published maps and information collected during field work). We aim to document the dominant hydrothermal alteration types affecting the area and the distribution of characteristic hydrothermal minerals associated to known ore deposits. Furthermore, pixels with similar spectral features to those associated

with ore-related hydrothermal alteration are intended to be highlighted, which may represent potential targets where unknown ore deposits may occur.

From a remote sensing perspective, we aim to conduct different ASTER image processing techniques, discard those images that provided little to no additional information and compare the results of those images with apparently useful data to assess whether they provide comprehensive and accurate information, based on our knowledge of the area and field verification. To extract the most useful spectral information from the ASTER bands and thus characterize geological features, different types of image processing techniques are applied: (1) Red-green-blue (RGB) band combinations, (2) band ratios and logical operators, (3) SWIR and TIR indices for mineral and lithologic mapping [22–24], and (4) PCA [25]. Overall, we intend to assess whether ASTER imagery processing is a valuable tool for mapping different lithological units, hydrothermal assemblages and key ore-related hydrothermal alteration minerals in the study area, which are difficult to distinguish with the available Landsat ETM+/OLI/TIRS images or aerial photos.

2. Geology

Sedimentary and igneous rocks crop out in the study area (Figure 3; Table A1). The ASTER scene can be divided geologically into three equal elongated areas parallel to the vertical limits of the scene (e.g., Figure 3). The western and central areas contain Siluro-Devonian to Tertiary sedimentary and igneous rocks, which correspond to the oriental flank of the Frontal Cordillera (e.g., Figure 3). The eastern area mainly contains modern sediments that have been deposited in the N-trending Calingasta-Uspallata Valley between the Frontal Cordillera (W) and the Precordillera (E of the geologic map and ASTER scene; e.g., Figure 3). The following paragraphs summarize the geologic units and their key lithologies present within these three areas (Figure 3).

The oldest units of the study area are marine shales, sandstones, conglomerates and carbonate facies from the Siluro-Devonian San Ignacio Formation and the Upper Carboniferous to lower Permian Agua Negra Formation [26,27]. The Tocota Pluton is a Permian granitic to tonalitic intrusive complex that intruded the Agua Negra Formation [21,26,27]. The Choiyoi Group is a Permo-Triassic volcano-sedimentary complex, which is the geologic unit with the largest outcrop surface within the central area of the studied ASTER scene. The Choiyoi Group has been divided into three formations: The Castaño Formation has conglomerates, sandstones and siltstones with volcanic facies (i.e., agglomerates, tuffs and andesite > rhyodacites); The Vega de los Machos Formation is a sequence of andesites, breccias, agglomerates, andesitic tuffs, ignimbrites, latites – dacites; and the El Palque Formation is a volcanic felsic sequence characterized by rhyolitic and rhyodacitic flows, ignimbrites, agglomerates and tuffs [26,28,29]. The geologic map in Figure 3 includes the Atutia Formation, as the youngest units of the Choiyoi Group, based on Heredia et al. 2002 [30]. This unit has been previously mapped as part of the Vega de los Machos Formation (e.g., [26,31]). The Mesozoic Intrusives are a group of plutonic to subvolcanic igneous bodies, which include a Triassic andesite porphyry and the Early Jurassic Las Vizcachas Granodiorite [26,28,30,31]. The Manrique Pluton is a Triassic granitic intrusive body, which we consider here as part of the Mesozoic Intrusives [29]. The Las Vizcachas Formation is a sequence of andesitic flows with minor agglomerates and lithic tuffs. It is Tertiary in age based on stratigraphic relationships (i.e., it is unconformably underlain by the Castaño and Vega de los Machos formations, and unconformably overlain by the Puntas Negras Formation) [26,30–32]. All the aforementioned units are located within the central area in Figure 3.

The geologic units covering the largest surface within the western area of the study ASTER scene/geologic map are the Puntas Negras and Atutia formations and locally, the Olivares and La Puentecilla formations. The Middle Miocene Puntas Negras Formation (Melchor Group) has tuffs, ignimbrites, pyroclastic flows, agglomerates and lapilli intercalated with basaltic, andesitic, dacitic and rhyolitic flows [26,27,32]. The late Miocene to Pliocene Olivares Group includes the andesitic basalts and basaltic andesites from the Olivares Formation. They are unconformably overlain by conglomerates, sandstones and siltstones from the Pliocene-Pleistocene La Puentecilla

Formation [26,31]. The most distinctive geologic unit within the eastern area is the alluvial fans shed from the active Andean orogenic front in the Holocene Rodeo-Calingasta Basin [26]. Locally, ignimbrites, andesites, tuffs, agglomerates, conglomerates and sandstones from the Miocene Lomas del Campanario Formation accumulated on the eastern foothills of Frontal Cordillera [32]. For further description of each unit see Table A1.

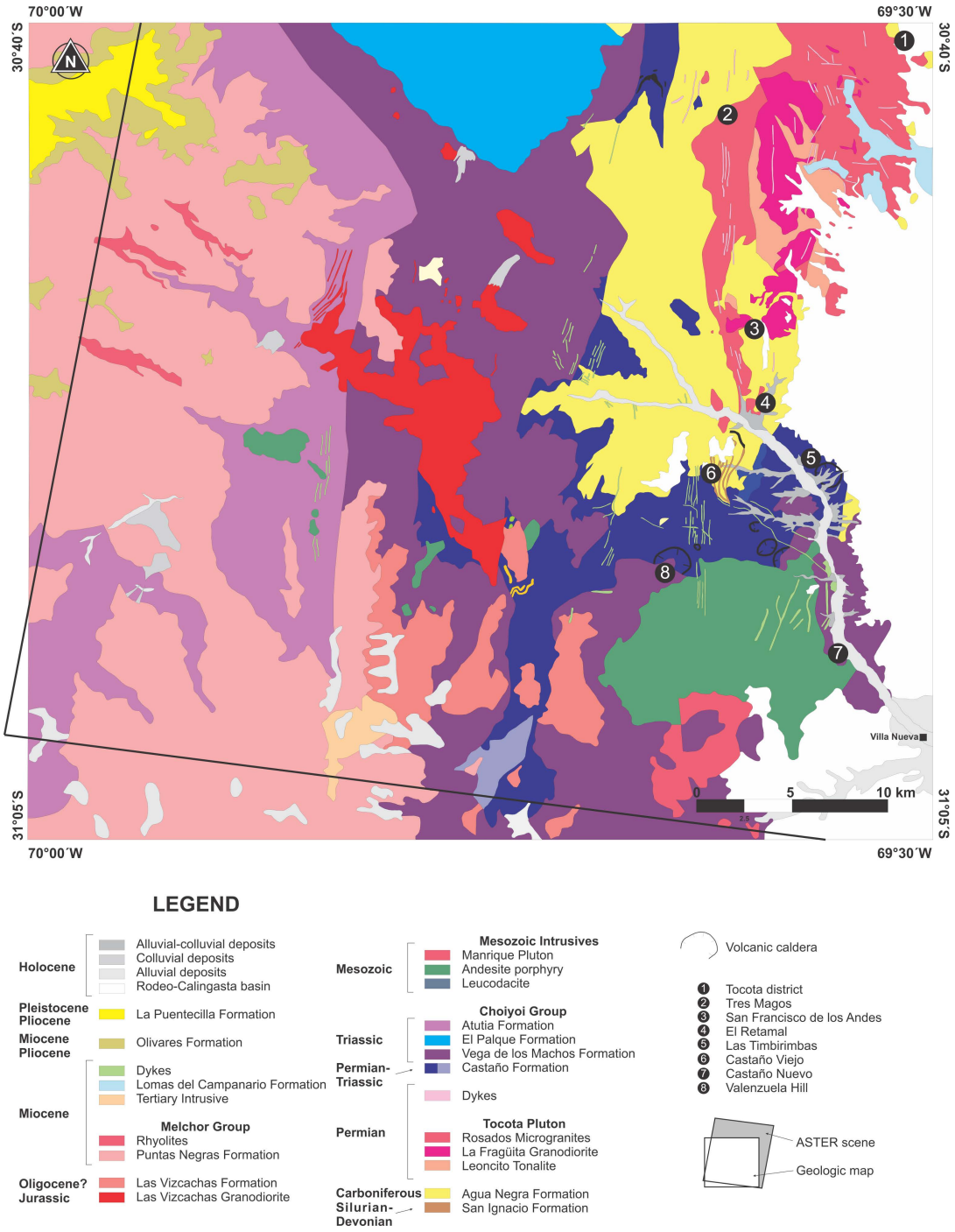

Figure 3. Geologic map of the study area [21]. This map has been drawn based on the available geologic maps [26,28,30,32] and field verification across the San Francisco de los Andes district.

3. Ore Deposits and Related Hydrothermal Alteration Zones

Key mineralized zones in the study area (Figure 3) include: (1) The Castaño Viejo district, a polymetallic vein system rich in Pb–Zn–Ag with a NNE-oriented hydrothermal alteration zone of approximately 10 × 6 km, characterized by sericite, secondary quartz and pyrite [26,33]; (2) The Castaño Nuevo district, a low sulfidation epithermal vein system with high Au–Ag grades, spatially related to argillic and silicic alteration zones [34,35]; (3) The San Francisco de los Andes district extends for over 30 km to the north of the Castaño River and has magmatic-hydrothermal tourmaline-cemented breccia pipes and veins that host Bi–Cu–Au mineralization [21,36–38]. In the vicinity of the San Francisco de los Andes mine, scarce epidote ± chlorite veins and tourmaline, magnetite and K-feldspar veins or hydrothermal replacement occur, whereas phyllic alteration is restricted to areas next to the breccia bodies or veins [21]. Kaolinite-rich argillic alteration occurs close to the Tres Magos mine [36]; (4) The As-rich Tocota district is characterized by arsenopyrite – pyrite – quartz – tourmaline veins and breccias. The principal ores extracted from the Krammer and Colo-Colo mines were Cu–As–Co-rich supergene minerals [36,39,40]. Concentric alterations close to Krammer grade from proximal quartz – sericite – jarosite-rich phyllic alteration to distal epidote – chlorite-rich propylitic alteration [40].

Discrete ore bodies and geochemical anomalies (Figure 3) are also located on the eastern flank of the Frontal Cordillera, including: (1) The El Retamal deposits, an area characterized by porphyry-style mineralization with Cu sulfides, molybdenite, scarce native gold and supergene Cu sulfates. The 7-km^2 area affected by hydrothermal alteration represents the NNE extension of the Castaño Viejo alteration zone. It is regionally altered to sericite, with clusters of strong silicic alteration, quartz – tourmaline alteration and restricted zones of potassic alteration [20,41]. (2) The Las Timbirimbas Ag–Au geochemical anomaly is an area where scarce mineralization has been documented. The surrounding area has been moderately altered to sericite, secondary quartz and jarosite, which has been superimposed on early formed tourmaline veins [20]. For a summary of key mineralogical, hydrothermal alteration and geological features in the aforementioned mineralized districts, ore deposits and geochemical anomalies see Table A2.

4. Methodology

4.1. Image Pre-Processing Techniques

An ortho-rectified ASTER image derived from level 1A data, without radiometric corrections, was provided by Servicio Geológico Minero Argentino (SEGEMAR). The scene was acquired on 19 March 2004 and was radiometric corrected using Abrams et al. (2002) [19] equation:

$$\text{Radiance bi} = (\text{DN value bi} - 1) \times \text{Radiometric conversion coefficient bi}$$

Radiometric conversion coefficients for each band bi were obtained from the metadata file of the scene (conversion coefficients for each band respectively in W/m^2·sr·µm are: b1 = 2.25, b2 = 1.89, b3N = 1.15, b3B = 1.15, b4 = 0.2174, b5 = 0.0696, b6 = 0.0625, b7 = 0.0597, b8 = 0.0417, b9 = 0.0318, b10 = 0.006882, b11 = 0.00678, b12 = 0.00659, b13 = 0.005693, b14 = 0.005225). The radiometric corrected bands were combined in two images, one for VNIR and SWIR bands (resampled to 15 m using nearest neighbor algorithm) and another for TIR bands (90 m spatial resolution).

The VNIR-SWIR image was atmospherically corrected using the module fast line-of-sight atmospheric analysis of spectral hypercubes (FLAASH) in ENVI 4.8. FLAASH uses MODTRAN4 radiation transfer models for the calculations [42,43]. This method has showed to be better than others for mineral mapping [44]. Atmospheric parameters (i.e., total water vapor and CO_2 concentrations) for the date of the scene acquisition were obtained from AIRS products, provided by the Goddard Earth Sciences Data and Information Services Centre (GES DISC, NASA). A mid-latitude summer (MLS) atmospheric model and 30 km visibility were used as parameters in the model. After the atmospheric correction, the resulting unit of the new imagery was reflectance. A visual inspection

of the spectral profiles for vegetation and minerals showed considerable improvement after the atmospheric correction.

4.2. Image Processing Techniques

Multiple techniques were applied to identify rock types, alteration assemblages and alteration minerals from the ASTER image: (1) RGB band combinations, (2) band ratios and logical operators, (3) Ninomiya's indices [22–24] and (4) PCA using raw imagery in digital number values [25].

4.3. SWIR Portable Instruments

SWIR data collected with portable instruments were used in this study to validate the results obtained by ASTER image processing techniques (field verification). The ASTER images presented in this article were compared against published and new field spectroscopy data from specific sites at El Retamal, Las Timbirimbas, Castaño Nuevo, Castaño Viejo and San Francisco de los Andes district (Figure 3). Spectra from two types of portable SWIR spectrometers were considered:

1. Spectra published by Delendatti and Bastías (2001) and Delendatti (2003) [20,41], collected with PIMA-SP™ for the Castaño area. This instrument was made by Integrated and Spectronics Pty. Ltd., Australia. It measures signals from 1300 to 2500 nm wavelength. Despite PIMA having a circular window of 1 cm diameter, the measured area is a strip of 1 × 0.2 cm. To produce a spectrum it takes approximately 25 s to measure a spot and 25 additional seconds to measure an internal standard [45]. Delendatti and Bastías (2001) published a series of reflectance PIMA spectra for the most commonly detected hydrothermal mineral assemblages at El Retamal [41]. Delendatti (2003) expanded the available reference data with reflectance SWIR spectra for pure minerals and mineral assemblages at El Retamal, Las Timbirimbas, Castaño Nuevo and Valenzuela Hill [20].
2. Over 600 air-dried, visually homogenous samples were measured every 500 m (approximately) across the San Francisco de los Andes district with TerraSpec™. This instrument was made by Analytical Spectral Devices, Inc. (ASD) Longmont, Colorado, USA and purchased in 2007 by CODES, University of Tasmania. TerraSpec collects data in a wider range (from 350 to 2500 nm) and from a larger area (2.5 cm diameter circle) than PIMA. The measurement time in TerraSpec depended on the darkness of each sample. The analyzed samples were medium to dark colored, as no sample had a strong argillic or sericitic alteration. The recommended measurement time it 4 to 6 s (light-colored samples), 6 to 10 s (medium-colored samples) and 10 to 20 s (dark samples) [45]. The optimization and white balance were conducted every 20 min approximately. Typically, three to four spots were measured on flat surfaces to consider any heterogeneity in the sample. The obtained mineral spectra collected with TerraSpec were interpreted with The Spectral Geologist™ (TSG) software version 7.

The SWIR profiles from pure species and mineral assemblages were compared to the laboratory spectra of every relevant mineral resampled to ASTER bandpasses after Mars and Rowan (2006), Baldridge et al. (2009) and Pour and Hashim (2012) [46–48].

5. Results: ASTER Spectral and Spatial Processing

The original ASTER raw data set was corrected according to the specific requirements for each of the four processing methods applied for this study: (1) RGB band combinations, (2) band ratios and logical operators, (3) SWIR and TIR indices for mineral and lithologic mapping [22–24] and (4) PCA [25].

As a general rule, Fe-oxides are mainly detected by bands 1 and 3. Al–OH-bearing minerals such as clay minerals, alunite, muscovite and illite exhibit absorption features in bands 5 and 6. Fe–OH mineral species such as jarosite and/or Fe-muscovite are detected by band 7, whereas Mg–OH and CO_3 mineral species such as chlorite, epidote and/or carbonates are detected by band 8 (Figure 4) [1,2,5,49–51]. In terms of alteration zones, a phyllic zone rich in illite – muscovite yields a

strong Al–OH absorption coinciding with ASTER band 6 (Figure 4). An argillic zone characterized by kaolinite and alunite collectively exhibits a secondary Al–OH absorption feature corresponding with ASTER band 5 (Figure 4). A propylitic zone with epidote, chlorite and calcite displays absorption features coinciding with ASTER band 8 (Figure 4) [1–5,47,48,50–54].

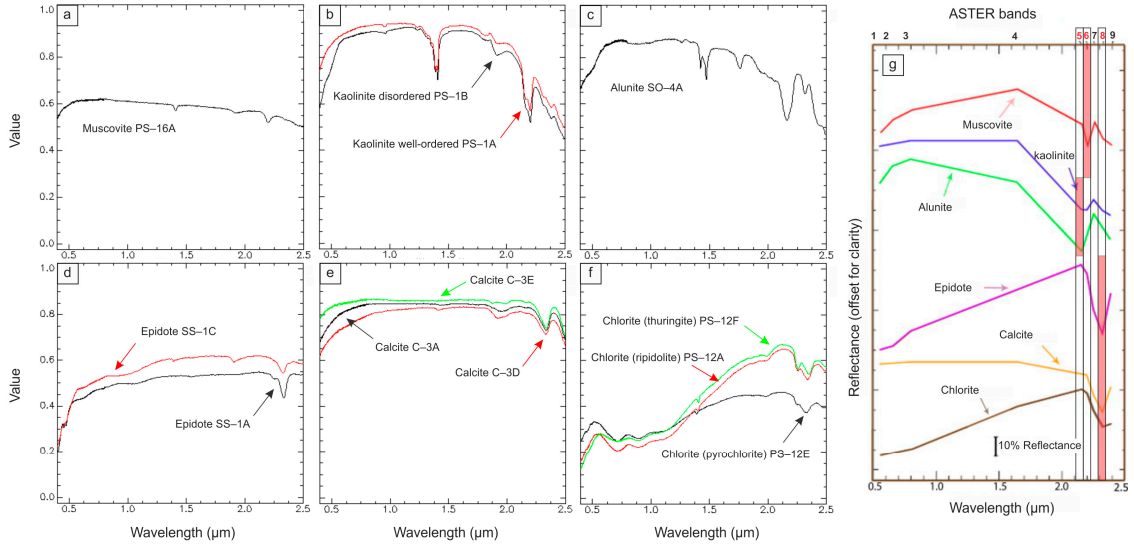

Figure 4. (**a**–**f**) Spectral signatures of muscovite, kaolinite, alunite, epidote, calcite, chlorite from the NASA Jet Propulsion Lab Spectral Library [46]. (**g**) Spectral signature of selected hydrothermal minerals resampled to ASTER bandpasses [48]. Band 5, 6 and 8 highlight kaolinite – alunite-rich argillic, mica-rich phyllic and epidote – calcite – chlorite-rich propylitic alteration zones (respectively).

5.1. False Color Composite Images—RGB Band Combinations

False color composite images with ASTER bands combinations (red, green, blue) provide a fast and expeditious method to detect the main lithological and hydrothermal alteration units. ASTER bands combinations (RGB) such as 468, 321 and 731 among others provide a rough guide to distinguish different geological features from a given area. Particularly, the false color composite image with ASTER bands 468 can be used as a hydrothermal alteration indicator (e.g., [55,56]). This SWIR band combination has been used to map alteration halos surrounding the Infiernillo porphyry copper deposit, Mendoza, Argentina and the propylitic and phyllic alteration zones in Qom province, Central Iran [49,57]. The ASTER band combination 468 (RGB) has no equivalent in Landsat ETM+ or OLI (Figure 1). Landsat ETM+ band 7 (2.064–2.345 µm) and OLI band 7 (2.107–2.294 µm) collects data in a broad portion of the electromagnetic spectrum. The ASTER bands 5 to 8 acquire spectral information within the same wavelength range than ETM+ band 7 and OLI band 7 (Figure 1; Table 1).

In the studied ASTER scene, false color composite images with ASTER bands 468, 321 and 731 (Figures 5, A1 and A2) highlight the location of felsic and intermediate igneous rocks, including the Tocota Pluton, Lomas del Campanario, El Palque rhyo-dacites, Manrique Pluton and the rhyolitic dykes, which can be distinguished from the mafic and sedimentary rocks on the ASTER scene (cf. Figure 3). Hydrothermal alteration associated with the Castaño Viejo district as well as other zones are also highlighted with these RGB band combinations. The false color composite image with ASTER bands 468 is the most comprehensive combination as it clearly differentiates argillic – phyllic alteration (pink) form silicic alteration (white), particularly in the Castaño Nuevo district. It is the only ASTER RGB band combination able to highlight the location of Krammer and Colo-Colo hydrothermal alteration zones (Figure 5).

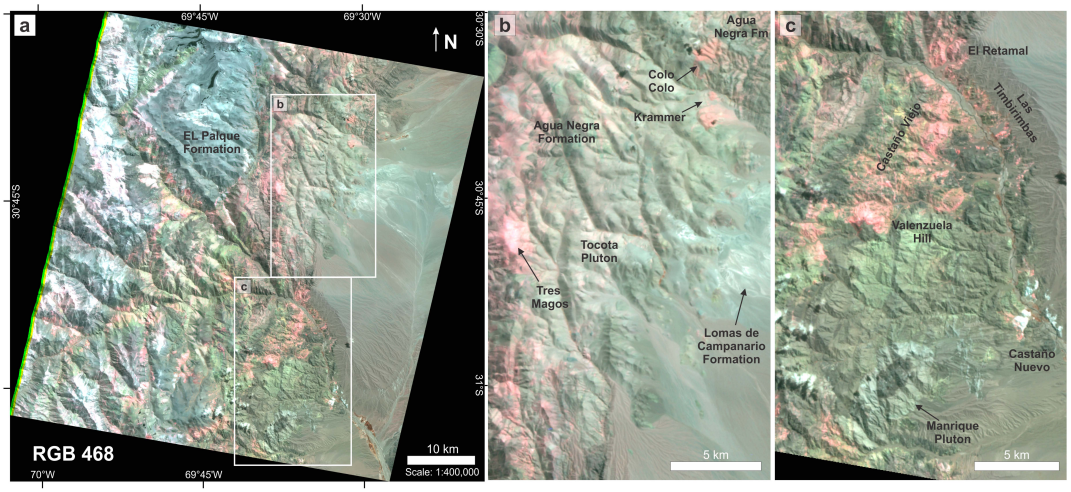

Figure 5. (**a**) False color composite image with ASTER bands 468 (RGB). (**b**) The San Francisco de los Andes district: Tocota Pluton (light green), Loma del Campanario (whitish green), Agua Negra Formation (dark green), Tres Magos alteration zone (whitish pink), and Colo-Colo – Krammer alteration zone (pink). (**c**) The Castaño area: argillic – phyllic alteration (pink), silicic alteration (white to light blue), Manrique Pluton and rhyolitic dykes (greenish blue). Compare the current ASTER imagery with the geologic map in Figure 3.

5.2. Band Ratios and Logical Operators

Selected ASTER band ratios and logical operators proposed in literature have proven to be useful to map specific geological features. Rowan and Mars (2003) [58] developed the ASTER VNIR band 2/1 ratio to detect the distribution of pixels with intense Fe^{3+} absorption, in the granitoids and gneisses in the Mountain Pass, California. This ratio expresses the reflectance decrease in band 1 relative to band 2, associated with ferric-iron absorption due to hematite – goethite-rich units [58]. Several studies have applied this VNIR band ratio with satisfactory results (e.g., [59–61]).

In the studied ASTER scene, the VNIR band ratio 2/1 successfully differentiates felsic to intermediate igneous rocks from both mafic igneous and sedimentary rocks (Figure 6; cf. Figure 3). In the upper left corner of Figure 6, the rhyolitic to rhyodacitic flows and ignimbrites from El Palque Formation are light to pale grey, contrasting with the Olivares basalts that are dark grey. The felsic Puntas Negras Formation and the overlying mafic Olivares Formation exhibit the same characteristics. In the lower right side, the Manrique granitic pluton and N- trending rhyolitic dykes are highlighted in bright pixels. The elliptical outcrop on top of the pluton is a roof pendant of the Vega de los Machos Formation (Figure 6; cf. Figure 3). The SWIR band ratio 4/6 is a good hydrothermal alteration indicator, which enhances the clay/mica response in the studied ASTER scene (Figure A3), as OH-bearing minerals exhibits high reflectance in band 4 and low reflectance in band 6 (Figure 4).

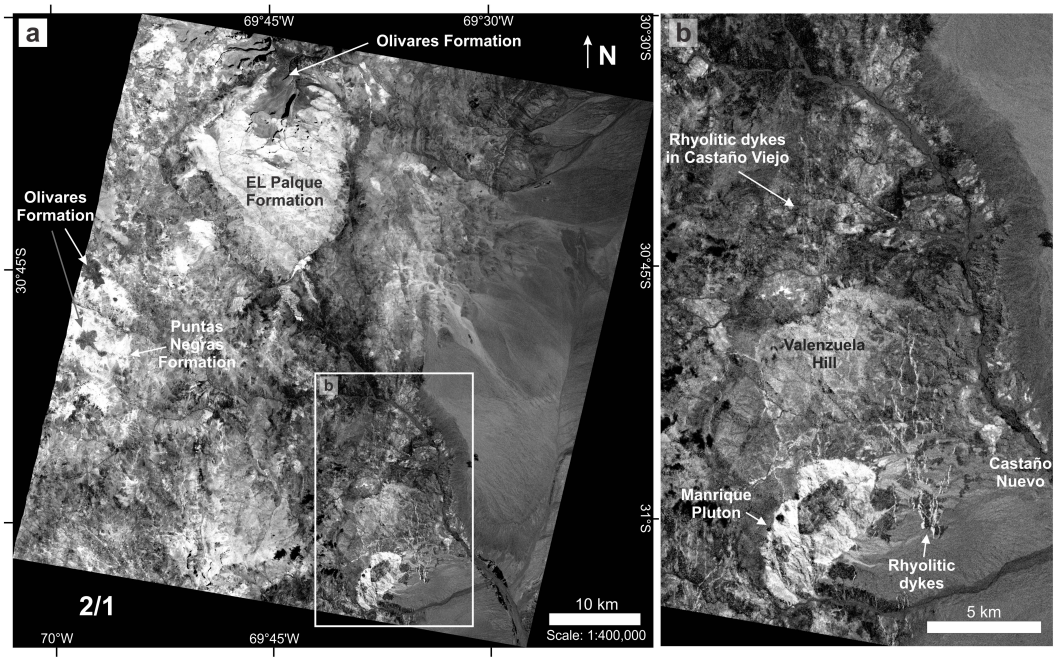

Figure 6. The ASTER band ratio 2/1 detects pixels with intense Fe^{3+} absorption [58]. (**a**) In the study area, it discriminates lithology types as it highlights felsic units in bright tones and mafic to intermediate rocks in dark shades. (**b**) The Castaño area: The Manrique Pluton and particularly the rhyolitic dykes are well-defined.

Rowan (2002) studied a porphyry copper-rich metallogenic belt in western Pakistan using Level 2 surface reflectance ASTER data without cross talk correction [62]. The author mapped sericite-rich phyllic zones using the band (5 + 7)/6 math operation and the argillic zones rich in alunite and/or kaolinite using (4 + 6)/5 [62]. Both logical operations have been applied successfully to detect illite, muscovite and/or smectite-rich zones and alunite, kaolinite and/or pyrophyllite-rich zones respectively (e.g., [58,60,61,63–65]). The resulting image from the ASTER bands (5 + 7)/6 math operation does not provide a good indicator for phyllic alteration in the study area. However, it successfully highlights muscovite-rich siltstones from Agua Negra Formation and only local hydrothermally altered phyllic zones (Figure A4, cf. Figure 3). The ASTER bands (4 + 6)/5 operation provides an accurate hydrothermal alteration indicator with detailed areas where it is likely to find alunite, kaolinite, pyrophyllite and illite (Figure A5).

The ASTER bands (4 × 7)/(8 × 8) operation with a linear enhancement was developed for this study. The reasoning behind this operation is that instead of focusing on the key spectral differences between micas and kaolinite group micas (i.e., wavelength absorptions within 2.185–2.225 and 2.145–2.185 μm, thus low reflectance in bands 6 and 5 respectively), we have focused on their similarities (Figure 4). Both micas and kaolinite group minerals exhibit high reflectance in bands 4 and 7 and low reflectance in band 8 (i.e., typical OH-bearing mineral absorption at ~2.2 μm; Figure 4). By multiplying bands 4 and 7 and dividing them by square of band 8 we aim to enhance these features and thus detect areas with both phyllic and argillic alteration. The proposed band math operation identifies the location of the Puntas Negras (W), El Palque (NW), Lomas del Campanario (NE) and Las Vizcachas (S) formations in dark shades (Figure 7; cf. Figure 3). The resulting image broadly highlights alteration zones rich in OH-bearing and clay minerals (bright pixels). At Castaño Nuevo, it detects argillic – phyllic alteration in bright pixels and the silicified zones in dark (Figure 7). The ASTER band (4 × 7)/(8 × 8) operation produces one of the most useful images for our study, as it provides robust information to differentiate not only lithologic units but also hydrothermal alteration types within only one image.

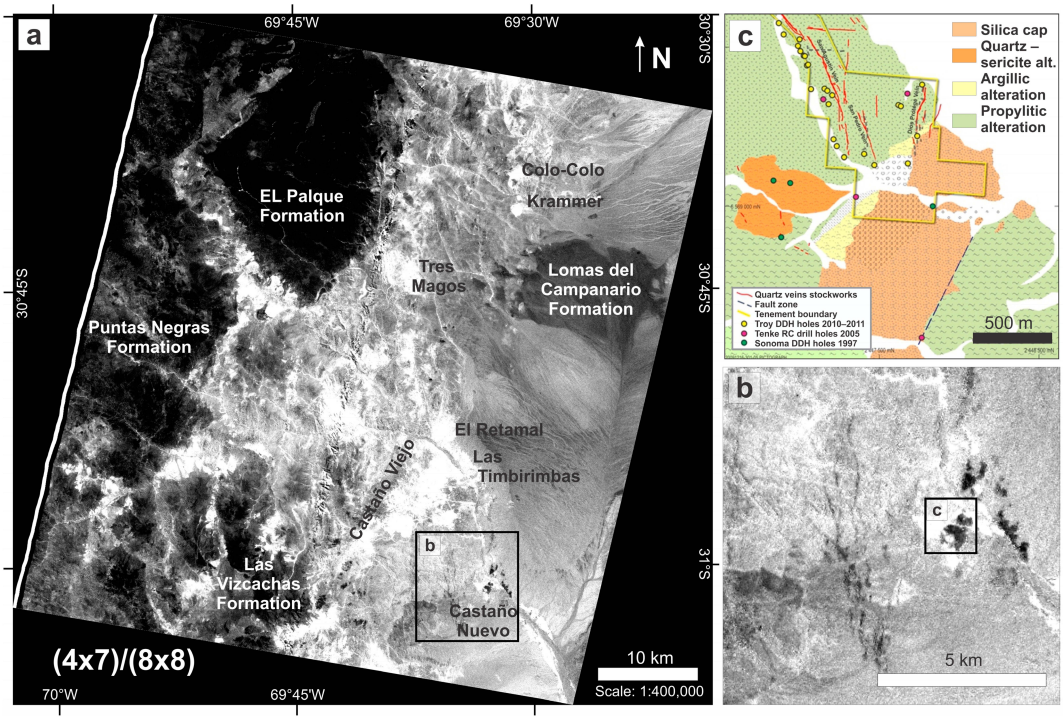

Figure 7. (**a**) The ASTER bands (4 × 7)/(8 × 8) operation was developed for this study to highlight areas with both phyllic and argillic alteration (bright pixels). This band math operation clearly identifies the location of the Puntas Negras, El Palque, Lomas del Campanario and Las Vizcachas formations (dark shades). (**b**) Enlarged image of the Castaño Nuevo district, which shows hydrothermal alterations rich in OH-bearing and clay mineral (light shades to white) and the more localized silicified zones and the N-trending rhyolite dykes (black to dark grey). The hydrothermal alteration zones mapped by the ASTER bands (4 × 7)/(8 × 8) operation are consistent with the alteration map proposed by Troy Resources Ltd. for the Castaño Nuevo area (**c**).

Pérez et al. (2007) [66] used the ASTER false color composite with band ratios 4/5, 4/6, 4/7 to highlight the hydrothermal alteration associated with El Pachón, Altares and La Coipa (San Juan province, Argentina) and Los Pelambres (Chile). This RGB combination was applied in the Bajo La Alumbrera-Andalgalá area (Cerro Atajo and Filo Colorado) in Catamarca province and at El Infiernillo porphyry deposit in Mendoza province, Argentina [49,63]. More recently, hydrothermal alteration zones from various porphyry copper deposits in Iran were successfully detected using this ASTER band ratio combination [56]. The RGB false color composite image of band ratios 4/5, 4/6 and 4/7 (Figure 8) is a useful tool for recognizing regional argillic – phyllic alteration zones and local silicic alteration in the Castaño Nuevo district. Clay- and mica-rich zones are highlighted in white to light blue colors near the known ore deposits as well as in apparently barren rocks (Figure 8). A clay/mica-rich alteration zone is recognizable at the base of El Palque rhyolitic flows and has affected the underlying Vega de los Macho Formation (Figure 8). Other areas with intense argillic and phyllic alteration assemblages can be distinguished to the west. The maroon color at Castaño Nuevo reflects intense silicic alteration (Figure 8; cf. Figure 7).

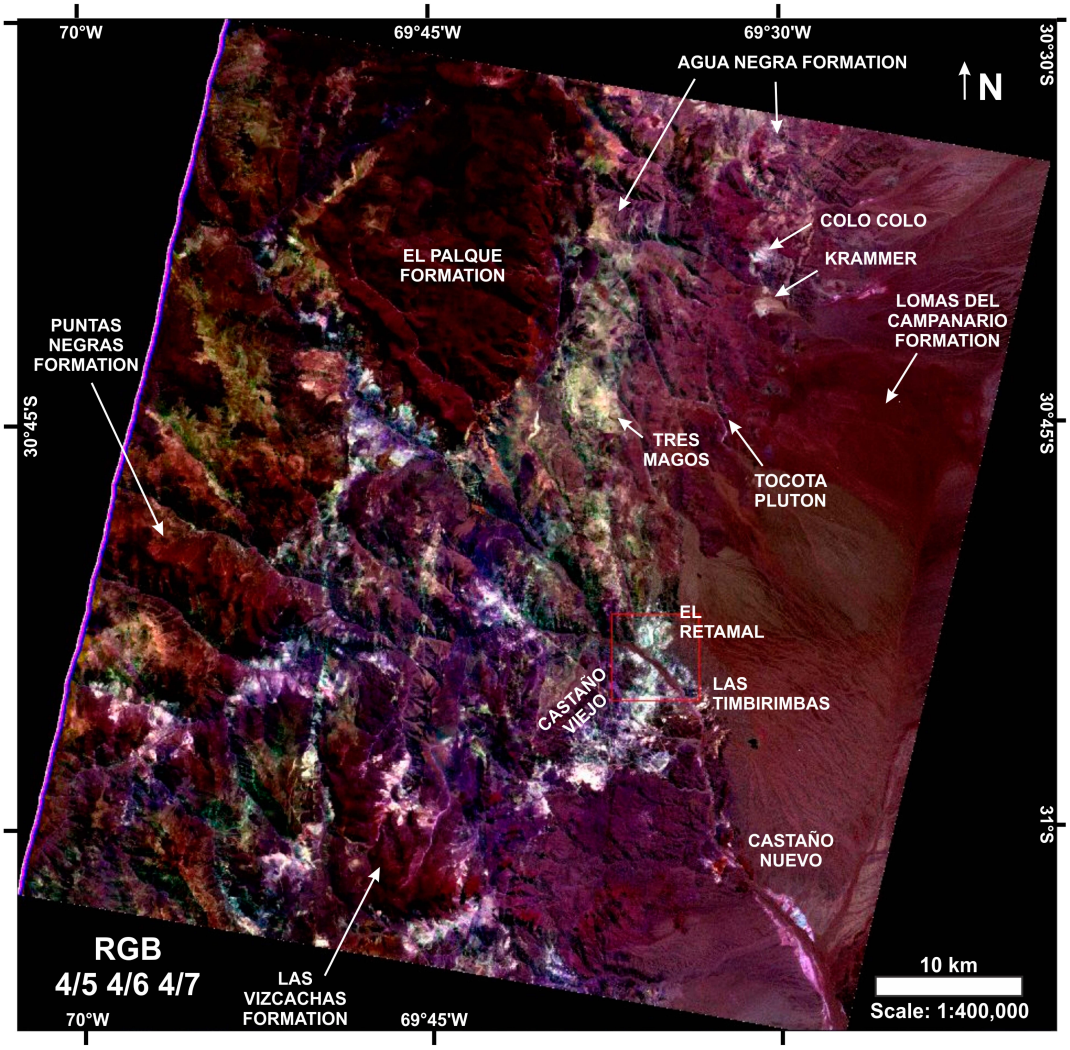

Figure 8. The ASTER false color composite image of RGB band ratios 4/5, 4/6, 4/7 represents a good discriminator of lithologic units (cf. Figure 3) and alteration types. It identifies the El Palque, Puntas Negras, Lomas del Campanario and Las Vizcachas formations and the Tocota Pluton (maroon shades). It differentiates the hydrothermal clays and micas (bluish white) from the mica- and clay-rich facies of Agua Negra Formation (greenish tones).

We have developed a false color composite image of ASTER band ratios that successfully outlines significant geological features in our study area. The ASTER RGB combination of band ratios 4/5, 4/7 and 3/1 with a linear stretch of 2% contrast displays an enhanced image that effectively differentiates the composition of lithologic units and the type of hydrothermal alteration (Figure 9). The reasoning behind this operation is that kaolinite has high reflectance in band 4 and low reflectance in band 5, whereas muscovite/illite has high reflectance in band 4 and relatively lower reflectance in band 7 (Figure 4). The band ratios 4/5 and 4/7 are expected to enhance the detection of argillic and phyllic alteration respectively. Although, bands 1 and 3 are traditionally used to detect Fe-oxide minerals, previous studies have documented contrasting spectral responses in felsic and mafic rocks based on these ASTER bands (e.g., [67]). Basalts have low reflectance in band 1 and higher reflectance in band 3, whereas granites have opposite spectral behavior (i.e., higher reflectance in band 1 and lower reflectance in band 3). The use of the band ratio 3/1 is conceived to aid documenting lithologic features, particularly highlighting granitic plutons from basaltic flows.

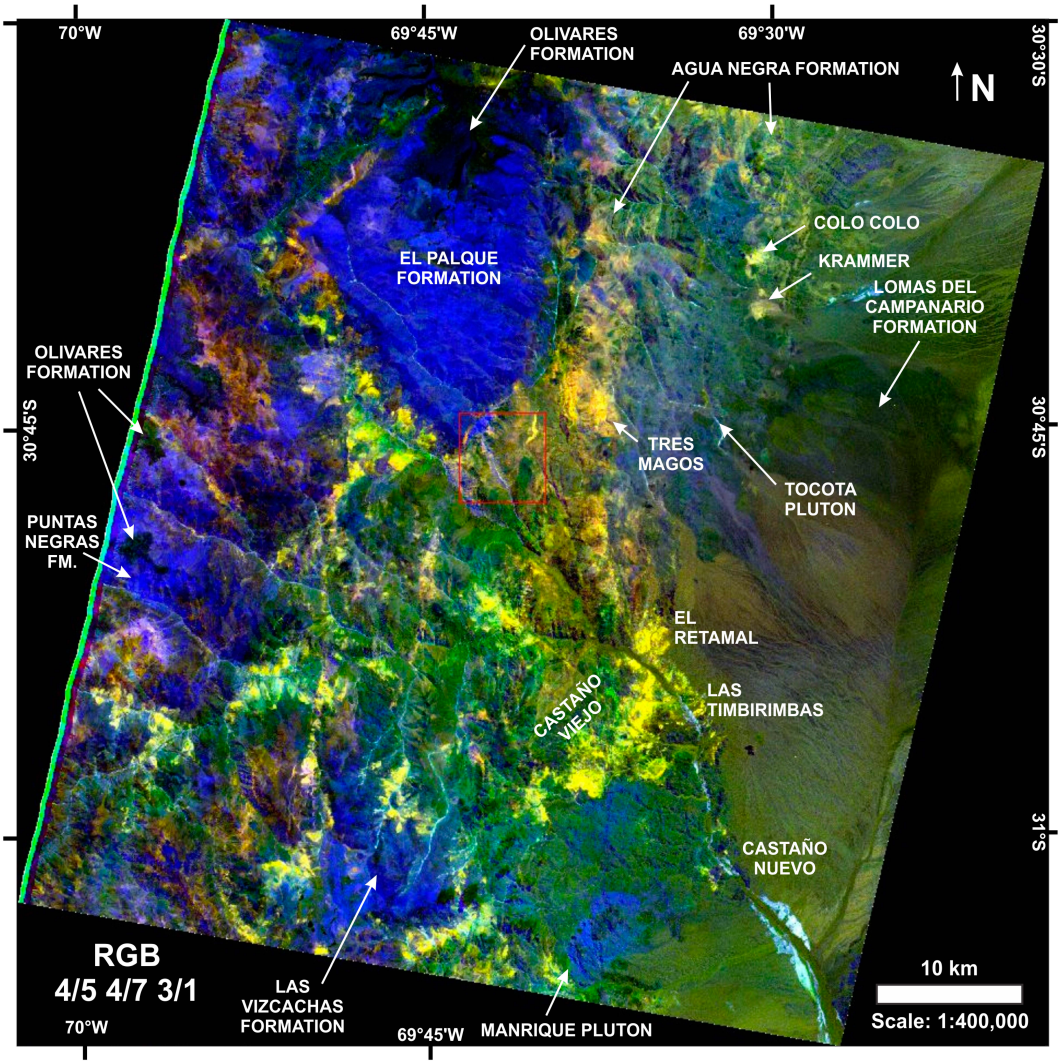

Figure 9. The enhanced ASTER band combination 4/5, 4/7, 3/1 with a linear stretch of 2% contrast was developed for the study area. Felsic units and silicified areas are shown in blue, whereas the phyllic and argillic alteration zones are highlighted in yellow. The intermediate volcanic to sub-volcanic rocks are shown in green, as are the Paleozoic and Mesozoic sedimentary units, whereas the basaltic lavas are dark green (cf. Figure 3).

In the study area, 4/5, 4/7 and 3/1 (RGB) best outlines significant geological features, effectively distinguishing lithologic units and types of hydrothermal alteration. It differentiates mafic (i.e., Olivares Formation) and felsic (i.e., Manrique and Tocota intrusive bodies and Las Vizcachas, Puntas Negras and El Palque formations) igneous rocks and sedimentary unit (Agua Negra Formation). The 4/5, 4/7, 3/1 RGB combination distinguished argillic – phyllic as well as silicic alterations. The proposed RGB band ratio combination is similar to 4/6, 4/7, 3/1 used by Di Tommaso and Rubinstein (2007) [49] and gives better results to aid geological and hydrothermal mapping for the study area.

5.3. SWIR and TIR Indices for Mineral and Lithologic Mapping

5.3.1. SWIR Indices

Ninomiya (2003) [22] defined a stabilized vegetation index with ASTER VNIR data, as well as several mineralogical indices using ASTER SWIR bands. The VNIR and SWIR indices have traditionally been applied to ASTER level 1B radiance at the sensor data without atmospheric corrections [22,23].

Zhang and Pazner (2007) [68] applied PCA to SWIR Ninomiya's indices to highlight alteration zones south of the Chocolate Mountains, California, USA. In the current study, atmospherically corrected ASTER data provides improved results.

The diagnostic spectral features of vegetation are very high reflectance in band 3, very low in band 2 and higher in band 1 [22]. OH-bearing minerals, mainly kaolinite, alunite and montmorillonite, are characterized by an absorption feature in band 6, resulting in high reflectance in band 4 and 7 and relatively low reflectance in band 6 [22,46,51]. Kaolinite has also an absorption feature in band 5, whereas alunite has absorption features in both band 5 and 8 [22,46,51]. Calcite is characterized by a strong and clear absorption feature in band 8 and a weak peak in band 5 [22,46,50,51]. Based on the aforementioned spectral features the OH-bearing minerals index (OHI), kaolinite index (KLI), alunite index (ALI) and calcite index (CLI) are defined as follow [22]:

$$\text{OHI} = (\text{band } 7/\text{band } 6) \times (\text{band } 4/\text{band } 6)$$
$$\text{KLI} = (\text{band } 4/\text{band } 5) \times (\text{band } 8/\text{band } 6)$$
$$\text{ALI} = (\text{band } 7/\text{band } 5) \times (\text{band } 7/\text{band } 8)$$
$$\text{CLI} = (\text{band } 6/\text{band } 8) \times (\text{band } 9/\text{band } 8)$$

Ninomiya (2004) [23] revised the OH-bearing minerals index (OHI), noting that both montmorillonite and the mica group have deep and sharp absorption features in band 6. He considered that OHI was suitable for detecting this group of hydroxyl minerals and renamed it OHI_a. A second group of OH-bearing minerals, including pyrophyllite, exhibits a deep and sharp absorption feature in band 5, therefore Ninomiya (2004) [23] defined a new OH-bearing minerals index (OHI_b) as:

$$OHI_b = (\text{band } 7/\text{band } 5) \times (\text{band } 4/\text{band } 5)$$

Kaolinite and alunite define a third group that has absorption features in bands 5 and 6 [22,23,46,51]. Both OHI_a and OHI_b are useful tools for detecting these hydroxyl-bearing alteration minerals.

The OHI_a is a better and more useful index than OHI_b for detecting alteration in the study area (Figure 10). The areas where it is more likely to find phyllosilicates are highlighted in white and correspond to the Castaño Viejo NNE alteration zone that goes from Valenzuela Hill to El Retamal and the more restricted Castaño Nuevo alteration zone (Figure 10c). To the north of Castaño River, the phyllosilicate-rich zones associated with El Retamal, Las Timbirimbas, Tres Magos, Krammer and Colo-Colo are highlighted white (Figure 10b,c).

In the OHi_a image (Figure 10) only the lower and intermediate section of the Choiyoi Group exhibit an evident mica-rich hydrothermal alteration. The Castaño and Vega de los Machos formations host the ore deposits and hydrothermal alteration associated with Castaño Viejo and Castaño Nuevo. Westward, the Vega de los Machos ± Atutia formations show alteration patches with OH-bearing minerals, even though no ore deposit is known to be associated with them (cf. Figures 3 and 10). The white outline surrounding El Palque Formation in Figure 10 highlights the area of intermediate volcanic rocks from Vega de los Machos Formation that has been likely altered to phyllosilicates. The light grey pixels between El Palque rhyolites and the Tocota Pluton mainly represent phyllosilicate-rich siltstones facies of Agua Negra Formation (Figure 10).

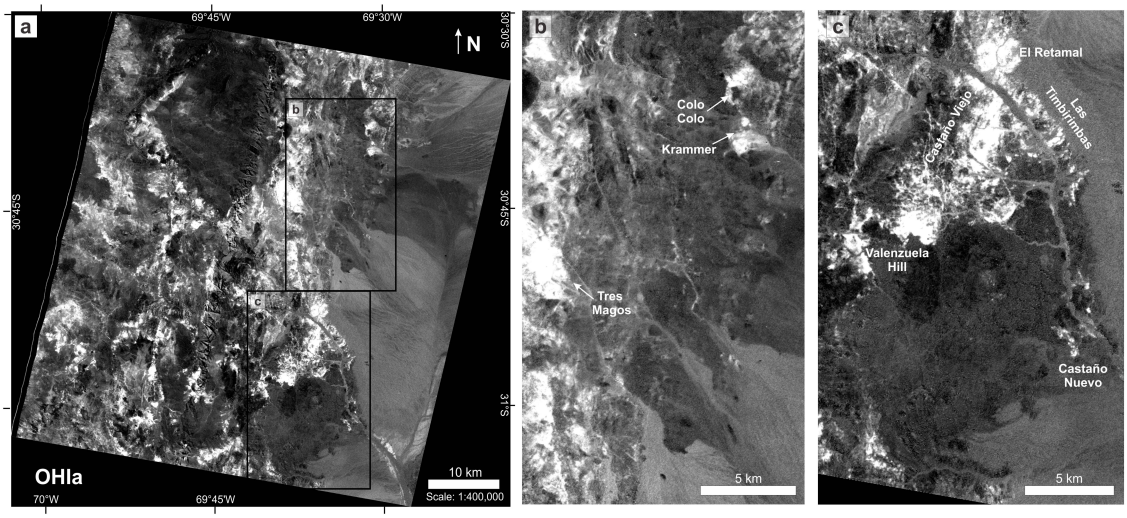

Figure 10. (**a**) OH-bearing minerals index image (OHIa), the white zones represent areas where it is more likely to find phyllosilicates. (**b**) The Tres Magos, Krammer and Colo-Colo alteration zones are highlighted white. (**c**) The NNE-trending Castaño Viejo alteration zone (from Valenzuela Hill to El Retamal and Las Timbirimbas) and the more restricted Castaño Nuevo alteration zone are detected in white.

The KLI image (Figure 11) yields similar responses to the OHI_a (Figure 10). This behavior is due to kaolinite, which is part of the third group of OH-bearing minerals with absorption features in bands 5 and 6. Most of the pixels classified as kaolinite in Figure 11 are likely to be muscovite and/or illite with kaolinite admixture.

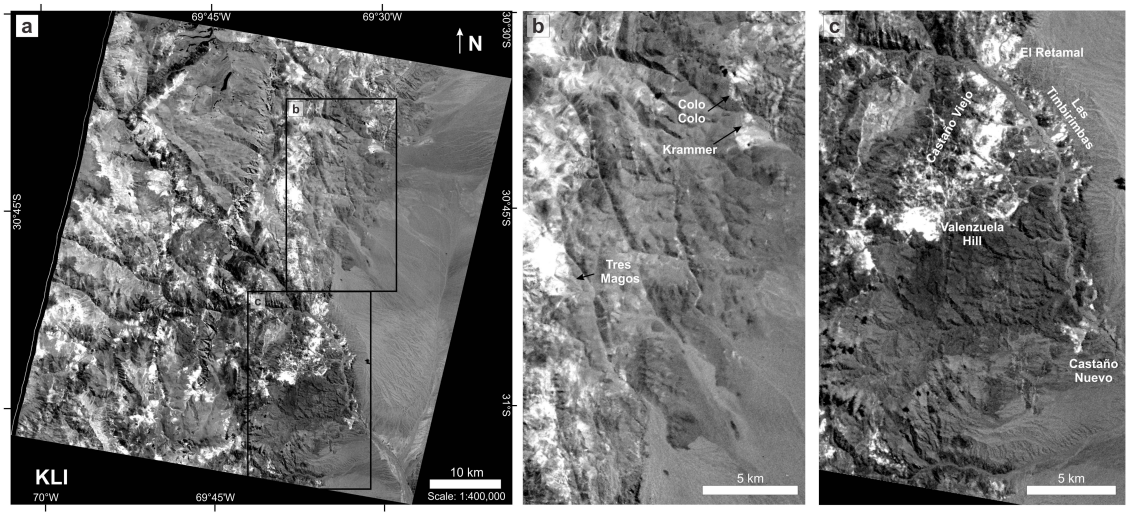

Figure 11. (**a**) Kaolinite index image (KLI), white zones represent areas where it is more likely to find kaolinite (±phyllosilicates). (**b**) The Tres Magos, Krammer and Colo-Colo alteration zones are highlighted white. (**c**) The NNE-trending Castaño Viejo alteration zone (from Valenzuela Hill to El Retamal and Las Timbirimbas) and the more restricted Castaño Nuevo alteration zone are identified in white.

The ALI image (Figure 12) displays a homogenous area with bright pixels at Valenzuela Hill but very diffuse elsewhere in the Castaño Viejo, Castaño Nuevo and Las Timbirimbas regions. At El Retamal, the spectral response to the ALI is very poor (Figure 12).

Calcite is not an abundant mineral inany of the geological units of the study area. This is reflected in the CLI image, which has no geological meaning and has been discarded.

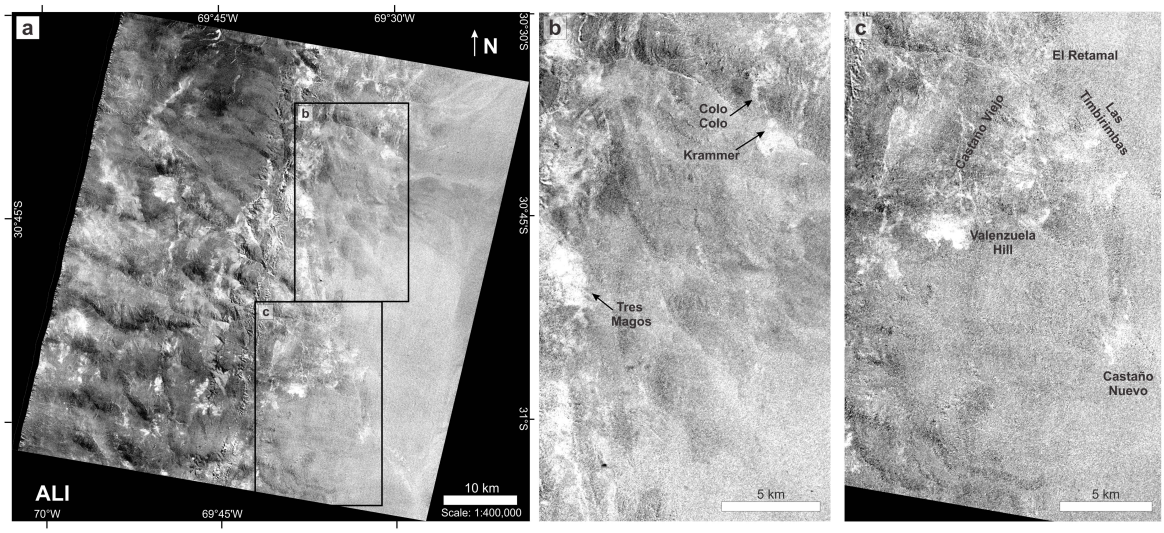

Figure 12. (**a**) Alunite index image (ALI), white zones represent areas where it is more likely to find alunite. The only hydrothermal alteration zones related to known ore deposits, which probably contain alunite based on dense clusters of white pixels are Tres Magos and Krammer to the north (**b**) and Valenzuela Hill to the south of the image (**c**).

5.3.2. TIR Indices

Ninomiya and Fu (2002) [24] proposed three indices for lithologic mapping using multispectral ASTER TIR remote sensing data. These are the Quartz Index (QI), Carbonate Index (CI) and bulk SiO_2 content Index (SI):

QI = (band 11/band 10)/(band 11/band 12)

CI = band 13/band 14

SI = band 12/band 13

The three lithologic indices were defined using Level-3A data without atmospheric corrections, which is radiometrically equivalent to the Level-1B radiance at the sensor data. The TIR indices have successfully proved their capability of mapping different geological units (e.g., [23,24,69,70]). Rockwell and Hofstra (2008) [71] applied QI and CI using ASTER Level-2 surface emissivity (Level-2B04) data to identify quartz and carbonates in northern Nevada, USA. Similar ASTER derived mineralogical indices using TIR data have been proposed to delineate quartz and mafic minerals contests for particular case studies (e.g., [72]).

Quartz is characterized by high emission in band 11 as a result of the clear absorption features in bands 10 and 12. Alkali (K- and Na-rich) feldspar exhibits much lower emission in band 11 as a consequence of a strong spectral peak in band 12 [5,23,46]. The QI is not strictly an identifier of quartz in rocks as it is strongly affected by the presence of alkali feldspar [23].

As the bulk SiO_2 content decreases, TIR emission for silica and silicate minerals and rocks shifts to longer wavelengths [73]. The band 12 to band 13 ratio for igneous rocks (or any other silicate rock) increases as the bulk SiO_2 content decreases [69]. This band ratio can be used to roughly distinguish felsic from mafic rocks. Carbonate and sulfate minerals can also be detected with ASTER thermal infrared data. Calcite and dolomite have an absorption feature in band 14 whereas gypsum has a very strong absorption feature in band 11 resulting in much higher emission in bands 10 and 12 [46,69].

When considering the three ASTER TIR indices proposed by Ninomiya and Fu (2002) [24], QI effectively discriminates the Tocota Pluton from the Agua Negra sedimentary rocks (Figure 13). The

different felsic facies from the Tocota Pluton contain abundant quartz and alkali feldspar, so the QI is relatively low producing the shades of dark grey in Figure 13. The sedimentary facies of Agua Negra Formation contain little or no alkali feldspar, resulting in very bright areas in Figure 13. The western, northern and southern limit of the Tocota Pluton are sharply defined, making this index a very effective mapping tool. The contacts between the Tocota Pluton and Agua Negra Formation are not clear in other satellite images or aerial photos; even the geologic map has simplified boundaries (cf. Figure 3).

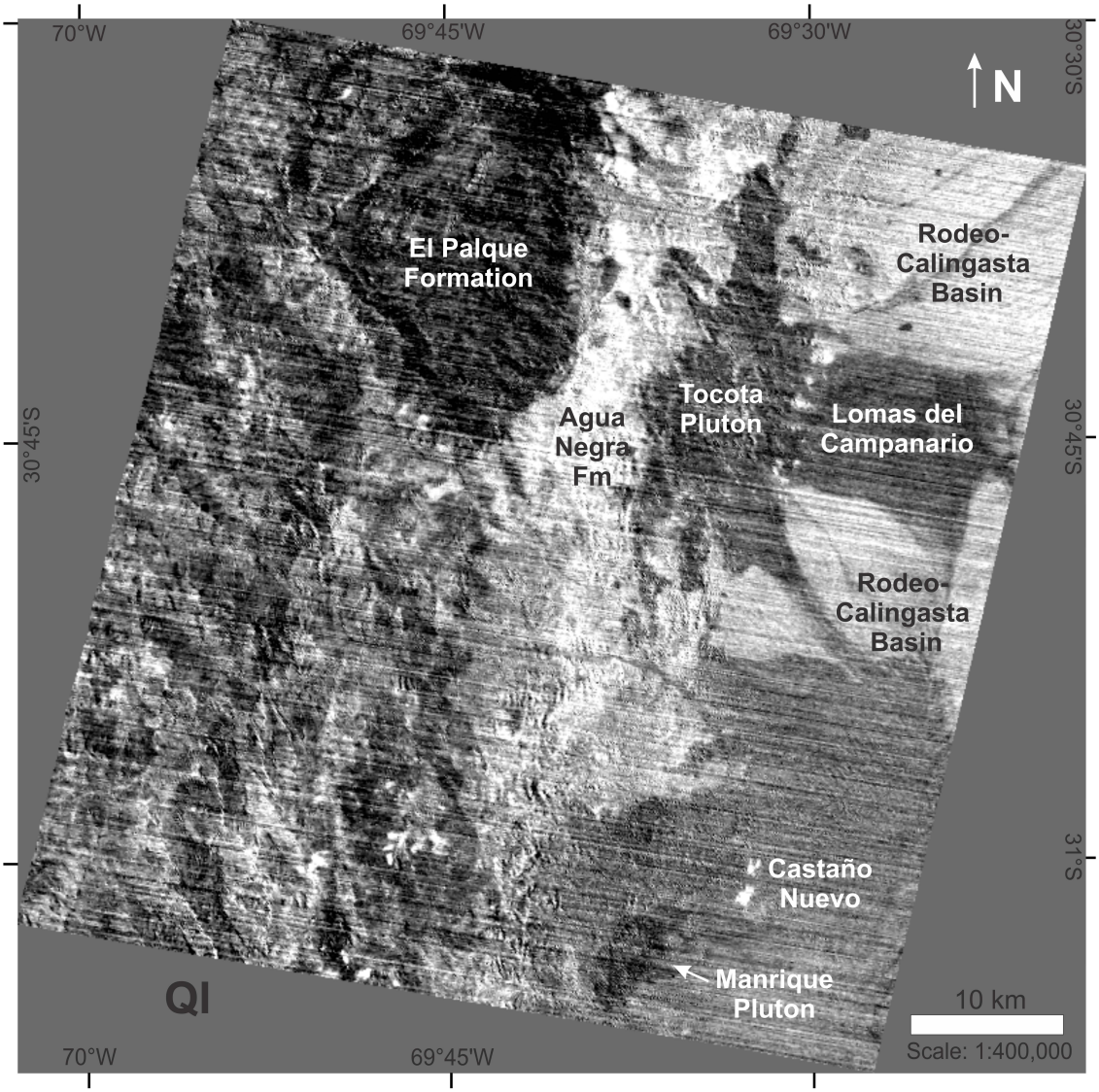

Figure 13. Quartz index image (QI). This ASTER TIR image is particularly usefully for detailed mapping of the limits of the Tocota Pluton and Lomas del Campanario Formation (dark grey). Alkali feldspar-poor sedimentary rocks from the Agua Negra Formation and the unconsolidated Quaternary deposits (at the base of Frontal Cordillera) are highlighted in light grey to white.

The north-eastern and south-eastern limit of the Tocota Pluton is covered by thick unconsolidated Quaternary gravel deposits accumulated at the base of the Andes (Figure 13). These sediments are rich in quartz but poor in alkali feldspar, resulting in light areas contrasting with the dark pixels of the Tocota Pluton. The eastern limit of the pluton is covered by the Lomas del Campanario andesite to dacite ignimbrites and tuffs (Figure 13; cf. Figure 3). These volcaniclastic rocks have a similar shade of grey to the Tocota Pluton making these units difficult to discriminate based on tonality (Figure 13).

The main feature that distinguishes both units is the rough texture of the Permo-Triassic igneous rocks against the smoother texture of the Miocene volcaniclastic rocks (Figure 13).

Both CI and SI were also calculated with the available ASTER TIR data. The CI is of little use as carbonate rocks, with calcite or dolomite, are very scarce in the study area. The SI response has no geological meaning and has therefore been discarded.

5.4. Principal Component Analysis

Topographic shading and albedo effects at the surface affect the radiant spectral flux measured by a remote sensor [25]. Principal component analysis is a robust statistical method that is used to suppress irradiance effects that dominate all bands, as a consequence the spectral reflectance is enhanced and geological features can be accentuated [25].

Pearson (1901) [74] invented PCA, whereas Hotelling (1933) [75] independently developed and named this method. It is based on a statistical transformation where an original set of data is reorganized following the greatest variability axes generating non-correlated components. The eigenvalues are a set of quantities defining the lengths of the principal axes and measuring the variability of the data. Eigenvectors are another set of data defining the direction of each axis and the correlation between the principal components (PC) and the original bands. The spectral properties from land cover, such as rocks, soils and vegetation responsible for the statistical variance recorded into each PC are indicated by the sign and magnitude of eigenvector loadings [7,65].

Feature-oriented principal component selection (FPCS) is a technique developed by Crosta and Moore (1989) [76] to map iron oxides and hydroxides related to sulfide ore bodies using Landsat TM. The 'Crosta technique' is an improvement of the FPCS method proposed by Loughlin (1991) [7] that has been successfully used for mineral targeting. It applies PCA to specific Landsat TM band sets in order to avoid mapping undesired features like vegetation, and making sure that the spectral information of alteration minerals is mapped into a single principal component (PC). The Crosta technique has become a standard tool for hydrothermal alteration mapping using Landsat TM/ETM+/OLI in regions with sparse or no vegetation and exposed bedrock such as the South American Cordillera [25]. This method has been effectively applied for mineral exploration (e.g., [20]).

Crósta et al. (1996) and Prado and Crósta (1997) [77,78] calculated PCs for high spectral resolution data to create mineral abundance maps. They effectively estimated the distribution of hydrothermal alteration minerals associated with gold mineralization in greenstone belt rocks using 24-band Geoscan data covering the VNIR, SWIR and TIR spectrum. Crósta et al. (2003) [25] applied PCA for the first time to ASTER imagery mapping alunite, illite, kaolinite + smectite and kaolinite in the Los Menucos epithermal gold prospect, Patagonia, Argentina. They selected four subsets of ASTER bands according to the characteristic spectral features of each group (Table 2). The PC that contains the target spectral information shows the highest eigenvector loadings from the ASTER band subset but with opposite signs [7,25]. Key hydrothermal alteration minerals have been successfully detected using this technique on ASTER imagery (e.g., [25,55,65,79]).

Table 2. ASTER band subsets for mapping alunite, illite, kaolinite + smectite and kaolinite based on PCA.

	Hydrothermal Alteration Minerals			
	Alunite	**Illite**	**Kaolinite + Smectite**	**Kaolinite**
ASTER bands	1	1	1	1
	3	3	4	4
	5	5	6	6
	7	6	9	7

The four groups of minerals listed in Table 2 were analyzed by PCA in the studied ASTER scene but only kaolinite, kaolinite + smectite and alunite exhibit patterns consistent with other techniques

and have geological significance (Figures 14 and 15; Figure A6). The eigenvector matrix in Table 3 shows the four PCs for kaolinite. Based on Loghlin (1991)'s and Crosta et al. (2003)'s criteria [7,25], PC4 contains the target information and enhances the presence of kaolinite.

Table 3. Eigenvector statistics for ASTER bands 1, 4, 6 and 7. PC4 shows a greater spectral contrast between bands thus minimizing the response from minerals other than kaolinite.

EIGENVECTOR	PC1	PC2	PC3	PC4
B1	0.305	0.562	0.548	0.538
B4	0.841	−0.241	0.207	−0.436
B6	−0.326	0.484	0.385	−0.714
B7	−0.303	−0.624	0.712	0.099

Principal component 4 has a high and positive loading from band 1 (0.538) and a high and negative loading from band 6 (−0.714; Table 3). The grey scale PC4 image exhibits dark areas with low DN values, these pixels most likely represent kaolinite. The information contained in every pixel was therefore multiplied by −1 to obtain an inverted PC4 image where kaolinite is displayed as bright pixels (Figure 14).

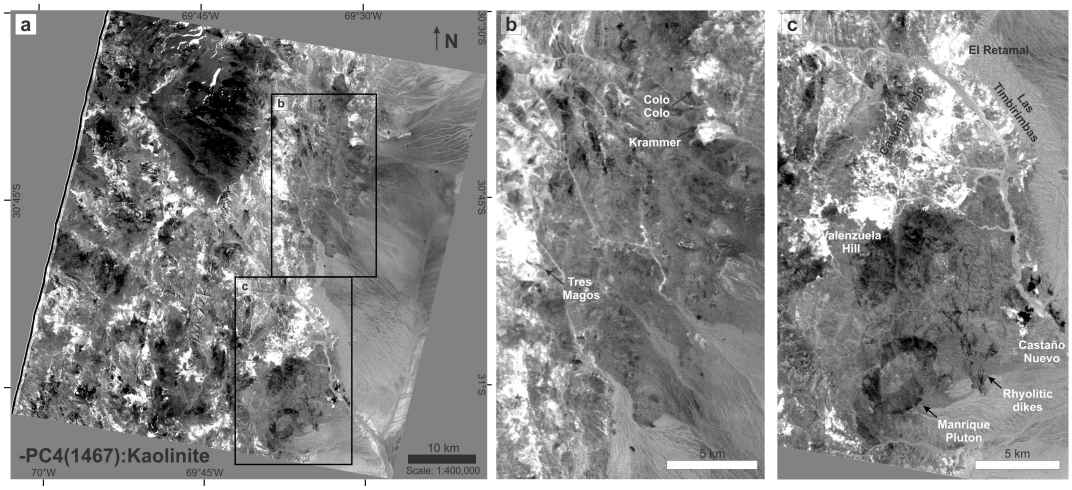

Figure 14. (**a**) Negated principal component 4 for bands 1, 4, 6 and 7 (kaolinite). The white zones represent areas where it is more likely to find kaolinite (±phyllosilicates). (**b**) In the northern portion of the ASTER scene the hydrothermal alteration associated to Tres Magos, Krammer and Colo-Colo are highlighted. (**c**) In the southern portion of the ASTER scene the hydrothermal alteration associated to the NNE-trending Castaño Viejo alteration zone (From Valenzuela Hill to El Retamal and Las Timbirimbas) and the more restricted Castaño Nuevo alteration zone are detected.

Based on previous field studies, coupled with band operators and Ninomiya's indices presented in this study, the bright pixels in Figure 14 are inferred to highlight areas rich in OH-bearing minerals and not just kaolinite. The dark areas in Castaño Viejo are interpreted to represent strongly silicic-altered rocks (Figure 14). The dark regions near Valenzuela Hill could be areas enriched with secondary quartz, or simply silica-rich facies in the andesitic porphyry (Figure 14).

The inverted PC4 for bands 1469 (kaolinite + smectite; Figure A6) shows similar areas as the negated PC4 for bands 1467 (kaolinite; Figure 14). The brighter colors match the areas where is most likely to find kaolinite + smectite but there are many areas with bright pixels where muscovite/illite is present instead of kaolinite and/or smectite. The silicic-altered areas in Castaño Viejo and the silica-rich facies in Valenzuela Hill are more evident with this PC. Felsic units such as the Manrique

Pluton or the N-trending rhyolitic dykes are highlighted in dark grey tones in both Figures 14 and A6 (cf. Figure 3).

Principal component 3, calculated for bands 1357 (alunite), detected smaller areas with hydrothermal alteration (Figure 15). The large NNE-trending hydrothermal alteration in the Castaño Viejo district is no longer evident in this image, with only a bright cluster of pixels located close to Valenzuela Hill. Another white cluster is located on the west limit of the Tocota Pluton close to the Tres Magos mine (Figure 15). The hydrothermal alteration zones rich in OH-bearing minerals in Krammer and Colo-Colo are not highlighted in Figure 15 due to alunite absence (cf. Figures 14 and A6).

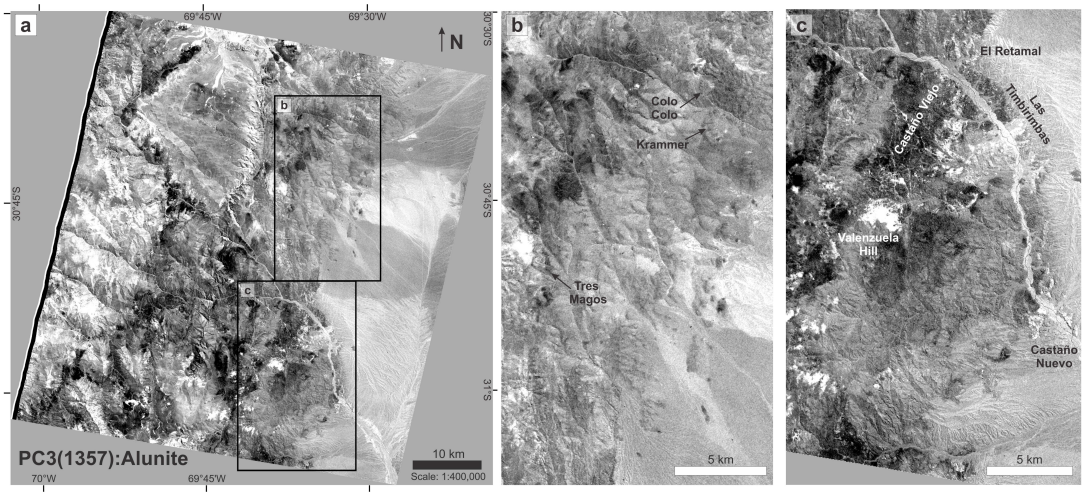

Figure 15. (**a**) Principal component 3 for bands 1, 3, 5 and 7 (alunite). White zones represent areas where it is more likely to find alunite. The only hydrothermal alteration zones related to known ore deposits, which probably contain alunite based on dense clusters of white pixels, are Tres Magos (**b**), and Valenzuela Hill (**c**).

6. Discussion: Field Verification

ASTER RGB band combinations, band ratios and math operators have provided semi-qualitative estimations of the hydrothermal alteration assemblages (not mineral abundance) and lithologic units present in the study area. However, Ninomiya's indices and Principal Component Analysis produced clear mineral abundance images that showed those areas most likely to contain key hydrothermal alteration minerals. The results obtained after processing ASTER imagery were compared to published field spectroscopy data [20,41], used here as field verification sites. The most characteristic PIMA spectra for El Retamal, Las Timbirimbas, Castaño Nuevo and Valenzuela Hill are shown in Figure 16. Our new field and spectroscopy data collected from verification sites within a radial distance of up to 4 km from the San Francisco de los Andes mine were also considered. However, hydrothermal minerals at San Francisco de los Andes are not abundant enough to be detected by ASTER, as they merely occur as veins, disseminated species and very localized massive replacement.

One of the most important issues to bear in mind during mineral and alteration mapping is the idea of mixed pixels, which are extremely common in hydrothermally altered areas. When working with ASTER data this is a common problem that affects the result (particularly dealing with the TIR subsystem, which has a 90 m spatial resolution and to a lesser extent SWIR with 30 m). The spectra presented in Figure 16 confirmed the presence of alteration mineral assemblages and thus the existence of mineral admixtures.

The Ninomiya's indices (Figures 10–12) are in agreement with the mineral assemblages detected by PIMA. The OH-bearing minerals index (OHI_a), highlighted the existence of mica group minerals and produced an image with bright pixels at El Retamal, Las Timbirimbas, Castaño Nuevo and Valenzuela Hill among other regions (e.g., Tres Magos) on the study scene (Figure 10). The PIMA

results confirmed the abundance of illite or sericite (S) in those four control areas (Figure 16). Although there is no available PIMA or TerraSpec analyses for the Krammer and Colo-Colo areas, this region exhibits potassic, propylitic and phyllic alteration zones [39]. Concentric porphyry-like alteration zones with a strong jarosite-weathered, quartz – sericite – pyrite core, grading to an intermediate alteration and outer propylitic alteration associated with quartz – tourmaline-cemented breccias were described by Machuca et al. (1994) [40]. In Figure 10 two evident phyllic zones with clear boundaries can be delineated in the Krammer and Colo-Colo areas. The southernmost zone coincides with the jarosite-weathered quartz – sericite – pyrite core mapped by Machuca et al. (1994) [40].

The kaolinite index detected the same areas as OHI_a but more restricted (Figures 10 and 11). Although some of the bright pixels in the scene are a response to the presence of kaolinite, others are due to muscovite – illite. Castaño Nuevo is the only area from the five control areas analyzed where kaolinite was consistently detected by PIMA (Figure 16). The remaining four areas have sericite or illite with jarosite as the most common alteration assemblage, frequently associated with tourmaline. Kaolinite has characteristic absorption features at band 5 (2.145–2.185 μm) and band 6 (2.185–2.225 μm) but only the last absorption is diagnostic for mica group minerals. Jarosite has a strong absorption feature in band 7 (2.235–2.285 μm), where kaolinite has a diagnostic reflection and so jarosite is not responsible for any interference.

Tourmaline group minerals have four absorption features between 2.150 and 2.400 μm. The exact positions vary considerably depending on the major mineral chemistry, thus wavelength positions are indicators of tourmaline species. The first peak, 2.200 μm, shifts due to Y-site substitution in the tourmaline lattice [80]. It is generally detected by band 6 but Na-rich tourmaline elbaite has an absorption peak as low as 2.173 μm. This feature would be detected by band 5 and potentially cause muscovite – illite + elbaite assemblage to be misinterpreted as kaolinite. Neither the PIMA studies performed by Delendatti and Bastías (2001) or Delendatti (2003) [20,41] detected 2.200 μm peak values low enough to be elbaite. Our detailed tourmaline chemical and TerraSpec analyses performed in samples from the San Francisco de los Andes district proved that most of the tourmaline species are schorl (Fe-rich tourmalines) and dravite (Mg-rich tourmalines) [21].

Most of the pixels classified as kaolinite are therefore more likely to be muscovite – illite with mineral admixtures. The phyllosilicate alteration minerals have a more regional and abundant distribution, whereas kaolinite is mainly found at the Castaño Nuevo district (Figures 11 and 16). There are no available PIMA or TerraSpec data and barely any references on the Bi–Cu Tres Magos mine. Angelelli (1984) [36] described 'kaolinitization' of Tocota granodiorite in the mineralized areas, which is consistent with the kaolinite index results, where a bright cluster of pixels is located close to the Tres Magos mine (Figure 11).

The alunite index showed a noticeable cluster of bright pixels in the Valenzuela Hill area (Figure 12). This is the only control area where alunite was consistently detected by PIMA studies (Figure 16) [20]. There is another clear bright cluster to the west of Tocota Pluton close to the Tres Magos mine (Figure 12). Although this area is particularly highlighted with ALI, it is also detected by OHI_a and KLI. Despite alunite shows a clear absorption feature in band 5, mica group minerals exhibit the same behaviors in band 6 and kaolinite in both bands. The presence of more than one mineral species causes interferences with the Ninomiya's indices. No SWIR spectroscopy is available for this area but the hydrothermal alteration is probably a mixture of clays and phyllosilicates.

Principal component analyses for kaolinite (1467) and kaolinite + smectite (1469) yielded results consistent with Ninomiya's OHI_a and KLI (cf. Figures 14 and A6; Figures 10 and 11). In a similar manner, PCA for alunite (1357) highlighted the same areas detected by ALI (cf. Figures 12 and 15). Ninomiya's indices are simple mathematical operations, whereas PCA is a statistic method to transform a set of multidimensional correlated variables into a set of linearly uncorrelated variables. Even though both techniques are based on completely different mathematical and statistical procedures, they exhibit a remarkably similar behavior for a given mineral or group of minerals. The Ninomiya's indices and

PCA results are also in agreement with the minerals detected by PIMA and TerraSpec, providing qualitative evidence to support the efficacy of the method.

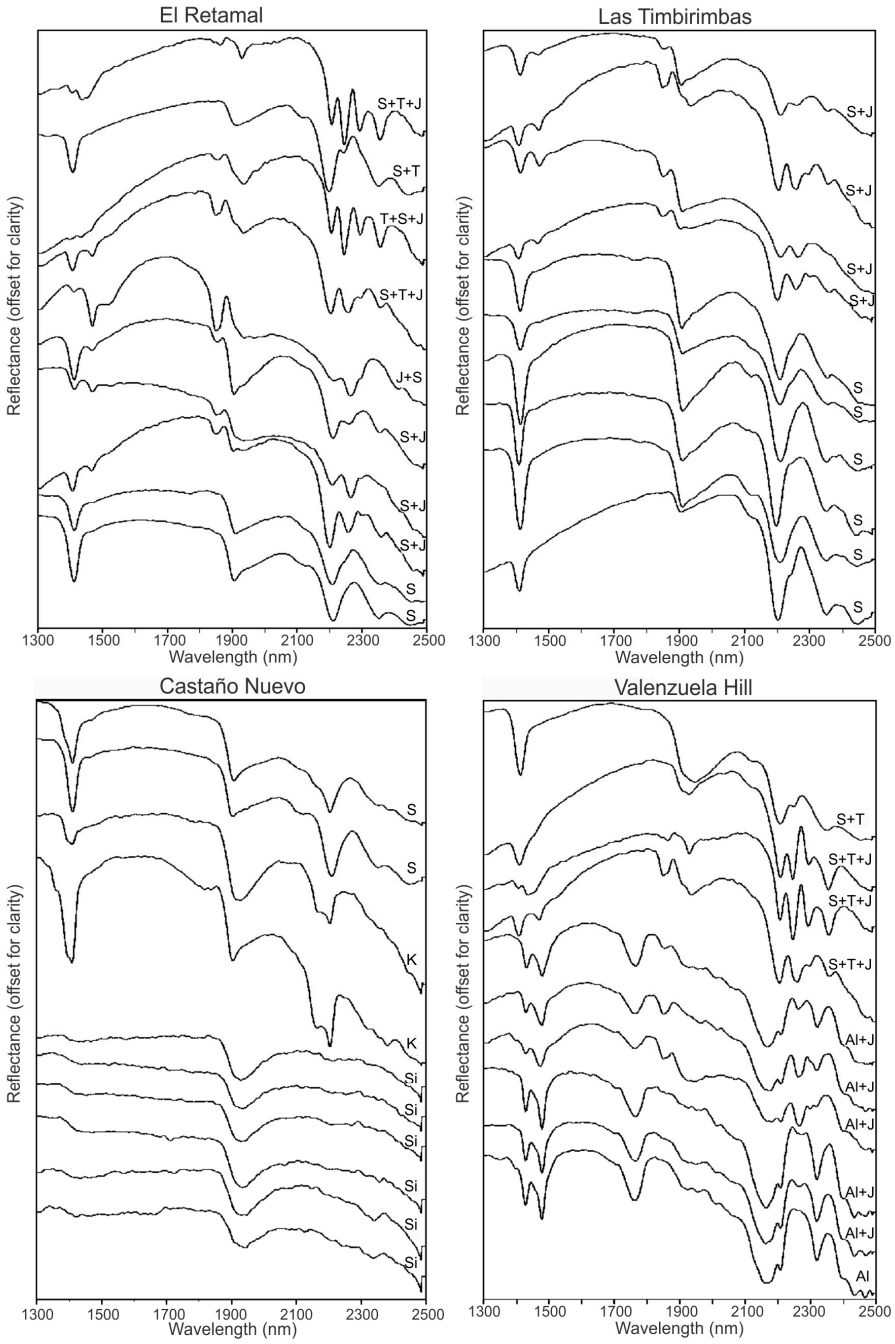

Figure 16. Most common PIMA spectra obtained from rock samples from El Retamal, Las Timbirimbas, Castaño Nuevo and Valenzuela Hill [20]. For the location of each area see the geologic map in Figure 3 and/or the ASTER products in this study. For further information regarding field localities and sample information see Delendatti (2003) [20]. The abbreviations for single minerals and mineral assemblages on each spectrum correspond to: Illite or sericite (S), tourmaline (T), jarosite (J), kaolinite (K), silica (Si) and alunite (Al).

Principal component analysis for alunite yielded much localized areas where alunite occurs, compared to kaolinite. Despite PCA for kaolinite and kaolinite + smectite showed contrasting results with PCA for alunite (Figures 14 and 15; Figure A6), common zones with bright pixel in the three

images are locally detected. Considering the spectral features of alunite and kaolinite are different in ASTER bands, those unique bright areas represent zones where sub-pixel mixing has occurred.

Although OH-bearing-minerals such as illite and kaolinite could be detected with TerraSpec in the San Francisco de los Andes district, their abundances are not high enough to be detected by the ASTER sensor. The phyllic and argillic alteration produced around the magmatic-hydrothermal breccia complex is not intense enough to be identified by the ASTER SWIR subsystem. In contrast, the phyllic and argillic hydrothermal alteration assemblages produced by epithermal (and locally porphyry-related) fluids are broad and abundant enough to be detected. At Castaño Viejo, El Retamal, Las Timbirimbas, Valenzuela Hill, Castaño Nuevo, Krammer, Colo-Colo and Tres Magos clays and phyllosilicates are the main components over areas larger than 30 × 30 m, and are thus detectable with the ASTER SWIR subsystem.

Table A3 lists the main lithologic and hydrothermal alteration features highlighted by each image presented in the current article. We have used this table to compare and contrast the results obtain by the ASTER processing methods applied during this study. In Table A3 we further discuss the results obtained based on our knowledge on the area and previous studies (i.e., both traditional geologic information based on field work, as well as Landsat TM and PIMA studies).

7. Conclusions

Image processing techniques are a powerful and cost-effective tool applicable during the first stage of mineral exploration. For this reason, the usage of multispectral sensors, such as ASTER and Landsat TM/ETM+—OLI/TIRS, has become a key additional procedure during the exploration stage for those mining companies with qualified specialists. For the past years, image processing techniques by themselves (or combined with other techniques such as airborne gravimeter and magnetic survey data) have led to successfully finding new ore deposits.

ASTER image processing of large areas has the ability to effectively discriminate smaller targets where it is possible to find mineral deposits. We believe it is critical to understand that interpreted hydrothermal alteration zones may not be real, so field verification is essential. When field data is not available, it is recommended to only consider interpreted alteration zones when having consistent results after applying several processing methods. The fact that an alteration zone is confirmed does not guarantee that the area is not barren or has metal concentrations high enough to make it economic for mining. For an interdisciplinary team or a specialist with a comprehensive knowledge of remote sensing and geology, ASTER processing techniques constitute a simple and effective method to map lithologic units and detect hydrothermal alteration assemblages that may be related to economic ore deposits.

In the current study area, processed ASTER imagery has proven highly effective at mapping hydrothermal alterations and lithologies in a section of the Argentine Frontal Cordillera. Although ASTER RGB band combinations, band ratios and math operators are good tools for obtaining a general idea of the geological and hydrothermal alteration features in an area, Ninomiya's indices and PCA were the techniques that provided the best and more comprehensive results regarding the occurrence of particular hydrothermal minerals. Both techniques helped to isolate areas where certain alteration minerals are present and overall to better highlight hydrothermal alteration zones. In conclusion, in the San Francisco de los Andes breccia-hosted Bi–Cu–Au mining district, very scarce illite, kaolinite and alunite were detected. Although epidote – chlorite veinlets are regionally disseminated in this area, their density is not high enough to be detected by ASTER. In contrast, clay- and phyllosilicate-rich alteration assemblages identified near the margins of the Castaño River and further south are spatially and genetically related with well-known epithermal and porphyry deposits. Regions with similar spectral responses were detected close to Tres Magos, Krammer and Colo-Colo, as well as to the left side of the ASTER scene. Those areas westward of the mining districts discussed in this article showed no correspondence with any known ore deposit, suggesting potential exploration opportunities to the west of the already identified mineral deposits.

We proposed the use of a new ASTER logical operation: $(4 \times 7)/(8 \times 8)$ and an ASTER RGB band ratio combination: 4/5, 4/7, 3/1, as both significantly highlighted not only the hydrothermal alteration affecting the area but also the different lithologies outcropping in the Frontal Cordillera. To the best of our knowledge, they have not been used in the past. We believe they will be useful in future studies, particularly in the Andes, as they provide both robust lithologic and alteration information within a single image. In summary, we have confirmed that ASTER imagery processing was a valuable tool for mapping lithological units in a portion of the Frontal Cordillera, otherwise difficult to distinguish with the available Landsat images or aerial photos. We have also interpreted the distribution of key hydrothermal alteration minerals and assemblages associated with known ore deposits and highlighted targets potentially related to economic mineralization that may be worth exploring in the future.

Supplementary Materials: The high definition file is available online at: https://zenodo.org/record/1163034#.WnF_mMlObDw.

Acknowledgments: The information published in this article is part of Francisco J Testa's PhD thesis. the main author wants to thank the AMIRA P1060 project, the ARC Research Hub for Transforming the Mining Value Chain (project number IH130200004) and the University of Tasmania—CODES, for providing funding for Francisco's PhD thesis and allowing the usage of licensed software, especially ENVI 4.8, ENVI 5.0 and ENVI FLAASH Atmospheric Correction Module. The senior author is grateful to CONICET for providing postgrad funding for the early stages of Francisco's PhD study as well as the Geology Department at Universidad Nacional del Sur and INGEOSUR for allowing the use of its facilities. The authors would like to thank the Servicio Geológico Minero Argentino (SEGEMAR) for providing the ASTER scene used in this study. Special thanks to Graciela Marin, Remote Sensing and GIS coordinator at SEGEMAR, for taking time to answer every question regarding the scene provided. The atmospheric data used in this study were acquired as part of the activities of NASA's Science Mission Directorate and are archived and distributed by the Goddard Earth Sciences (GES) Data and Information Services Centre (DISC). Last but not least, we gratefully acknowledge the three anonymous reviewers selected by Remote Sensing who examined the original manuscript; their critical reading and valuable comments greatly improved this article.

Author Contributions: This article represents a joint effort from the team of authors. Francisco J. Testa conceived and designed the study and wrote the paper. Francisco J. Testa and Cecilia Villanueva worked together during ASTER data preparation, analysis and interpretation; David R. Cooke supervised the work and was involved during the geological interpretation of the processed ASTER data and provided valuable ideas for the discussion, as well as edited the entire manuscript. Lejun Zhang provided relevant suggestions about the scientific content and reasoning when processing PIMA and TerraSpec data, as well as editorial assistance.

Conflicts of Interest: The authors declare no conflict of interest.

Appendix

Table A1. Summary of geologic units present in the study area (cf. Figure 3) based on selected literature [21,26–32]. Key features including age, lithology type, and spatial relationship between units are included in this stratigraphic table. Geologic units are listed in order of increasing age, the youngest at the top and the oldest at the bottom.

Unit Name and Age	Description	Spatial Relationship with Other Units	Interpretations and/or Additional Comments
La Puentecilla Formation • Pliocene-Pleistocene age	A 600 m-thick sedimentary sequence of conglomerates, sandstones and siltstones	It unconformably overlies the Olivares Formation (Figure 3)	Alluvial fans shed from the active Andean orogenic front
Olivares Formation • Late Neogene: late Miocene to Pliocene age	A series of andesitic basalts and basaltic andesites	The 300 m-thick massive flows are unconformably underlain by Puntas Negras Formation and were intruded by dacitic to rhyodacitic bodies (Figure 3)	–
Lomas del Campanario Formation • Miocene age	Ignimbrites, andesites, tuffs, agglomerates, conglomerates and sandstones of up to 950 m thick	Unconformably overlies the Tocota Pluton to the west; Most of this unit accumulated on the eastern foothills of Frontal Cordillera (Figure 3)	–
Melchor Group: Puntas Negras Formation • Middle Miocene age • The middle-upper part of Punta Negra Formation yielded K–Ar ages of 15.6 $\pm$ 1.3 Ma and 13.4 $\pm$ 2 Ma (unspecified mineral)	1500 to 2000 m-thick sequence of tuffs, ignimbrites, pyroclastic flows, agglomerates and lapilli; The pyroclastic materials are commonly intercalated with basaltic, andesitic, dacitic and rhyolitic flows	The volcaniclastic sequence is unconformably underlain by the Vizcachas Formation, Vizcachas Granodiorite, Choiyoi Group and Tocota Pluton (Figure 3)	• The younger sedimentary facies of the Melchor Group (i.e., Rio Mondaca Formation) are not exposed in the study area; • The Las Vizcachas Formation is considered to be the oldest unit of the Melchor Group by Heredia et al. (2002) [30]
Las Vizcachas Formation • Controversial Upper Permian age based on a 255 $\pm$ 5 Ma K–Ar whole-rock age in andesite [29] • Either Jurassic or Oligocene-Miocene age based on its stratigraphic position between the Choiyoi Group and the Melchor Group [26,31]	300 to 400 m-thick package of massive andesitic flows with minor agglomerates and lithic tuffs	It is unconformably underlain by the Castaño and Vega de los Machos formations; It is unconformably overlain by Puntas Negras Formation (Figure 3)	More likely to be Tertiary in age as it has only been affected by Andean compressive tectonics; The strong unconformity separating the Choiyoi Group from Las Vizcachas Formation appears to reflect the fossilization of the prior extensional period
Granitic Intrusives • Triassic	A group of granites, leucomicrogranites and rhyolitic porphyries	The **Manrique Pluton** is the only Granitic Intrusive outcropping in the study area (Figure 3)	We consider the Triassic Granitic Intrusives part of the Mesozoic Intrusives

Table A1. *Cont.*

Unit Name and Age	Description	Spatial Relationship with Other Units	Interpretations and/or Additional Comments
Mesozoic Intrusives: Las Vizcachas Granodiorite • Early Jurassic age based on a 200 ± 7 Ma K–Ar age (unspecified mineral)	A group of plutonic to subvolcanic igneous bodies associated with the Choiyoi Group. The Las Vizcachas Granodiorite and an andesite porphyry are the largest Mesozoic intrusives exposed in the study area (Figure 3)	This N-trending tonalite to granite complex, to the NW of the andesite porphyry, has intruded the Vega de los Machos and Castaño formations, and it is covered by volcanic rocks from the Tertiary Melchor Group to the north (Figure 3)	Based on Pearce tectonic setting discrimination diagrams this unit formed in a calc-alkaline continental magmatic arc
Mesozoic Intrusives : Andesite porphyry • Triassic age		Intruded the Choiyoi Group, particularly the Vega de los Machos and Castaño formations (Figure 3)	The genetic relationship with the Manrique granitic pluton to the south is unclear, because profuse hydrothermal alteration masks the contact between both Mesozoic intrusives [29]
Choiyoi Group: El Palque Formation • Absolute ages range from 267 ± 5 to 233 ± 10 Ma	An acidic volcanic sequence with mainly rhyolitic and rhyodacitic flows, ignimbrites, agglomerates and tuffs	A 1500 m-thick sub-horizontal rhyolitic flow is exposed as a triangular outcrop between the San Francisco and Las Leñas rivers (Figure 3)	• The Choiyoi Group accumulated during a rifting event associate with normal faulting caused by the beginning of the rupture of Gondwana, and its thickness decreases eastwards due to the Tocota Pluton horst; • Collapse calderas have been documented to the south of the Castaño River in the Castaño Formation (Figure 3), which represent the Choiyoi Group's volcanic edifice roots located on top of buried magmatic chambers; They correlate with the exposed Tocota Pluton to the north of the river
Choiyoi Group: Vega de los Machos Formation • Permo-Triassic unit: • Lower Permian age based on a 289 ± 19 Ma Rb–Sr whole-rock isochron age and a 288 ± 5 Ma K–Ar plagioclase age • Middle Triassic age based on 243.8 ± 5 and 234.6 ± 4.5 Ma K–Ar ages (unspecified mineral)	Andesites, breccias, agglomerates, andesitic tuffs, ignimbrites and minor latites and dacites	It overlies the Castaño Formation (Figure 3)	
Choiyoi Group: Castaño Formation • Permian age	Sequence of polymict orthoconglomerate intercalated with agglomerates, tuffs, and andesitic flows; Sandstones and siltstones with volcanic components, andesites and minor rhyodacites to rhyolites are common in the middle levels; Limestones with chert nodules intercalated in the volcanic facies characterize the upper levels	The volcano-sedimentary Choiyoi Group unconformably overlies the Agua Negra Formation (Figure 3)	

Table A1. *Cont.*

Unit Name and Age	Description	Spatial Relationship with Other Units	Interpretations and/or Additional Comments
Tocota Pluton: The Leoncito Tonalite, La Fragüita Granodiorite, Rosados Granite, and related N-oriented dykes • Permian based on Rb–Sr ages on primary biotite-whole rock pairs (269.1 ± 1 to 267.2 ± 1 Ma; Roadian to Wordian stage), and U–Pb zircon ages (Kungurian to Wordian stage)	North-elongated plutonic to sub-volcanic complex with a rough centripetal compositional zonation, where the younger and more acidic facies occur toward the center	Intruded the Agua Negra Formation (Figure 3); It is the southernmost extension of the Colangüil Batholith	Post-orogenic extensional pluton
Agua Negra Formation • Upper Carboniferous to lower Permian age based on fossil plants (*Rhacopteris ovate* and *Gondwanidium platinum*), and marine invertebrate (*Cancrinella* sp. and *Orthoceras* sp.) assemblages	Shales, sandstones, conglomerates and limestones	The 2000 m-thick sedimentary sequence is unconformably overlaying the San Ignacio Formation (Figure 3)	The Carboniferous sediments were deposited in a back arc basin where deltaic system transitioned to open marine conditions; whereas the Permian sequence was accumulated in a retroarc foreland basin
San Ignacio Formation • Siluro-Devonian age based on spore type in the marly facies	Limestone, dolomite and marly-limestone intercalated with shales	Very localized outcrops south of the Castaño River (25 to 70 m- thick overthrust sequence); Basement of the study area (Figure 3)	A shallow-water carbonate platform

Table A2. Summary of key mineralogical, hydrothermal alteration and geological features that characterize known ore deposits and geochemical anomalies located within the studied ASTER scene. Table based on selected literature [20,21,26,33–40].

District, Deposit Type and Occurrence	Location	Common Ore and Gangue Minerals	Grades	Host Rocks	Hydrothermal Alteration
Castaño Viejo • Polymetallic vein system • Center-south: Base metal-rich veins have an approximate E-trend; Only San Nicolas and Animas veins are particularly enriched in silver • North: Silver-rich San Ignacio vein system and neighboring veins have variable orientations	Located to the south of the Castaño River (Figure 3)	Argentiferous galena, sphalerite, chalcopyrite, chalcocite, covellite, tetrahedrite and pyrite; Carbonates and quartz are the main gangue minerals	• Center- south: Only the San Nicolas and Animas veins are Ag-rich • North: Silver-rich San Ignacio vein system (2–6 kg/t Ag) • The inferred and indicated reserves at Castaño Viejo are 0.8 mt @ 3–9% Pb, 1–7.4% Zn, 114–507 g/t Ag, < 1% Cu and < 2 g/t Au	• Center-South: The Permo- Triassic volcaniclastic rocks of Castaño Formation • North: Carboniferous sedimentary rocks of Agua Negra Formation and locally both the the Siluro- Devonian San Ignacio Formation and the Permo-Triassic San Ignacio rhyodacite	• To the east of the N-trending cluster of Triassic rhyolitic dykes, there is a distinctive NNE hydrothermal alteration zone: The 10 km long and 6 km width alteration domain extends from Valenzuela Hill to El Retamal (Figure 3); This zone is characterized by silicic, pyritic and sericitic alteration proximal to the vein system and distal propylitic alteration • Geochemical assays from Secretaria Minera de la Nación identified several Cu and Mo anomalies; To the north, west and south of the Castaño Viejo district, alteration zones with consistent Cu, Mo, Pb and Zn geochemical anomalies were documented by Gonzalez Amorin et al. (1968, 1969)
Castaño Nuevo • High grade, low sulfidation epithermal Au–Ag veins • Between 1890 and the 1950s, three veins were exploited at Castaño Nuevo: 1- Dios Protége, a NNE-trending vein of > 370 m length and 3 m wide, which likely extends north across the Castaño River; 2- The NW-trending St Agustin vein system, located 700 m west of Dios Protége, has been mined over 150 m strike, with widths of 1–3 m; 3- Southwest from St Agustin is the San Pedro vein with limited historical mining	Located 7 km downstream from Las Timbirimbas (Figure 3)	Quartz–adularia with late amethyst and very low sulfide contents	• Argentinean government records indicate an average grade of 20 g/t Au [34] • In December 2009, Troy Resources Argentina Ltd acquired 100% legal right over the Castaño Nuevo project; Ten assays yielded gold grades with values below 10 g/t Au except for a 15 cm sample containing 27 g/t Au. The gold–silver ratio is about 1:1 [34]	Choiyoi Group: Vega de los Machos Formation	The quartz vein systems are associated with argillic and silicic alteration zones to the south; According to Troy Resources Limited's website, these large zones of argillic alteration and silicification represent hot spring-style hydrothermal alteration that occurred at the paleosurface, implying a shallow epithermal level; The entire district, including the quartz vein system to the north and the hydrothermal alteration to the south, covers an area of 2.5 x 2.5 km
San Francisco de los Andes (SFDLA) • Magmatic- hydrothermal tourmaline-cemented breccia pipes and veins are spatially associated with the Tocota Pluton; • Southern domain: San Francisco de los Andes, Amancay, Cortaderas, Esmeralda, Pingo, Martina Chapanay and La Fortuna-Chorillo mines; • Central domain: Los Tres Magos, Mary, Santa Barbara, Larry, Mirkokleia, Rodophis, San Roque and Flor de los Andes deposits; • The Northern domain includes the Dos Amigos and Ranqueles mines and it is comparable with the As-rich Tocota district described by Wetten (1999) [39]	The district extends for over 30 km to the north of the Castaño River (Figure 3) • The San Francisco de los Andes mine is located 5 km north from the Castaño River, and the Tres Magos mine 11.5 km NNW from San Francisco de los Andes (Figure 3)	• San Francisco de los Andes is the largest Bi deposit hosted in a hydrothermal breccia complex in Argentina; It has complex Bi–Cu–Pb–Zn–Mo–As–Fe–Ag–Au mineralization, including native elements, sulfides, and sulfosalts; • At Tres Magos, the mineralization hosted in the granodiorite occurs as supergene Bi- and Fe-arsenates coatings	• The SFDLA deposit was sporadically mined (1940s – 1980s); Production reached 112 t of ore and bismuth concentrates; 2,420 t of mineral with 3–6% Cu and 1.2–4.5% Bi [36] • In 1990, Aguilar Mining Company estimated a resource of 0.15 Mt with 5% Cu, 1.2% Bi, 200 g/t Ag for the 35 m thick supergene zone; Although the total depth of the breccia complex is unknown, it was identified a hypogene zone with grades of 0.8% Cu, 0.6% Bi, 80 g/t Ag, and 4 g/t Au at depths between 35 and 80 m	The Bi–Cu–Au mineralized structures are hosted within the Tocota Pluton and adjacent sedimentary rocks of the Agua Negra Formation • At Tress Magos, the geological features are similar to the ones at San Francisco de los Andes, with tourmaline-bearing quartz veins and aplitic dykes crosscutting the granodiorite and sedimentary units	• At San Francisco de los Andes deposit, hydrothermal alteration around the tourmaline breccia complex is characterized by scarce mm-thick epidote veins with associated chlorite; Tourmaline, magnetite and K-feldspar occur as veins or hydrothermal replacement in more restricted areas; Illitic and silicic alteration is restricted to areas next to the breccia bodies or veins [21] • At Tres Magos, kaolinite-rich argillic altered granodiorite was documented by Angelelli (1984) [36]

Table A2. *Cont.*

District, Deposit Type and Occurrence	Location	Common Ore and Gangue Minerals	Grades	Host Rocks	Hydrothermal Alteration
Tocota • As-rich veins • Three mineralized structures: 1- Sub-vertical arsenopyrite – pyrite – quartz – tourmaline-rich veins commonly striking E (NE and NW locally), 5–60 cm width and < 50 m depth; 2- A NW-trending quartz – tourmaline-cemented breccia dyke is 10 to 30 m thick and 1300 m long; 3- Small tourmaline-cemented breccia outcrops (a few m long) associated with the vein system	Located on the eastern limit of the Frontal Cordillera, 5 km east of Tocota town (Figure 3); The most important mines of the district include Krammer and Colo-Colo, close to Tocota, as well as Ranqueles and Chimborazo in the northern part of the district	The principal ores extracted were Cu–As–Co-rich supergene minerals • Common hypogene minerals in the vein system are pyrite, chalcopyrite, Co-rich arsenopyrite, pyrrhotite, marcasite, cassiterite, sphalerite, gold, quartz and tourmaline; Supergene minerals include covellite, chalcocite, digenite, arsenates, jarosite and goethite; • The NW-trending breccia dyke contains quartz, tourmaline, arsenopyrite, jarosite, hematite and supergene copper minerals	As-rich veins were mined between 1943 and 1952; The average grades ranged between 20 and 30% As; The minable reserves exceed more than 37,500 t, equivalent to 5000 t As; The annual As productions for 1943 and 1944 were 1050 t and 850 t As respectively • The maximum gold content in the vein system is 5 g/t and in the breccia facies 0.34 g/t	The mineralized structures are hosted in the Agua Negra Formation and locally close to the contact with the Tocota Pluton	• Moderate to low Intensity • Potassic, phyllic, local intermediate argillic and more regional propylitic alteration zones • Lara et al. (1993) linked the NW-trending breccia dyke with blind porphyry copper deposits • A buried mineralized porphyry body was interpreted based on induced polarization (IP) anomaly; Concentric alterations close to Krammer: strong quartz – sericite – jarosite-rich phyllic alteration in the center, grades outwards to an Intermediate alteration and distal epidote – chlorite-rich propylitic alteration [40]
El Retamal • Porphyry-style mineralization, which occurs as veins and disseminated ore	Located to the north of the Castaño River (Figure 3), after the confluence of the Atutia and San Francisco rivers	Supergene Cu sulfates and hypogene molybdenite identified at the surface (Quebrada Seca), and hypogene chalcopyrite, molybdenite and pyrite at depth (both disseminated and veinlets); Bornite, chalcocite, aresnopyrite and marcasite are less abundant, and disseminated native gold is rare	Selected intervals in diamond drill cores yielded high Au grade of up to 6 g/t	Aguan Negra Formation and the Tocota Pluton	The hydrothermal alteration zone covers 7 km^2 and represents the NNE extension of the Castaño Viejo alteration system; The Leoncito Granodiorite and Agua Negra Formation are regionally altered to sericite; Strong silicic alteration clusters and very localized potassic alteration are common, but less abundant than the sericitic alteration; Quartz – tourmaline alteration was overprinted by late stage illite, quartz, pyrite, jarosite, goethite and traces of hematite
Las Timbirimbas • Geochemical and geophysical anomalies	Located along the Castaño river banks (Figure 3), downstream from El Retamal and upstream from Castaño Nuevo	Geochemical and geophysical anomalies detected, but scarce mineralization has been documented (quartz, pyrite and sulfates)	—	Choiyoi Group: Castaño Formation	Andesites, tuffs and rhyodacites have been moderately altered to sericite, secondary quartz and jarosite; This hydrothermal alteration is superimposed on early formed tourmaline veins

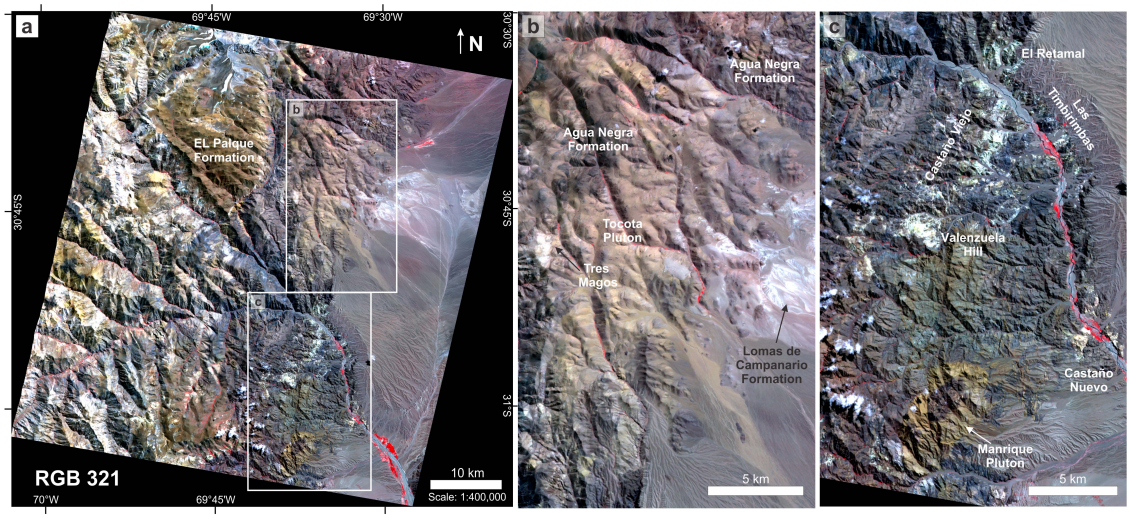

Figure A1. (**a**) False color composite image with ASTER bands 3, 2, 1 (RGB). (**b**) The San Francisco de los Andes district: Tocota pluton (orange brown), and Loma del Campanario (white). (**c**) The Castaño area: argillic – phyllic and silicic alterations (whitish color). Compare the current ASTER imagery with the geologic map in Figure 3.

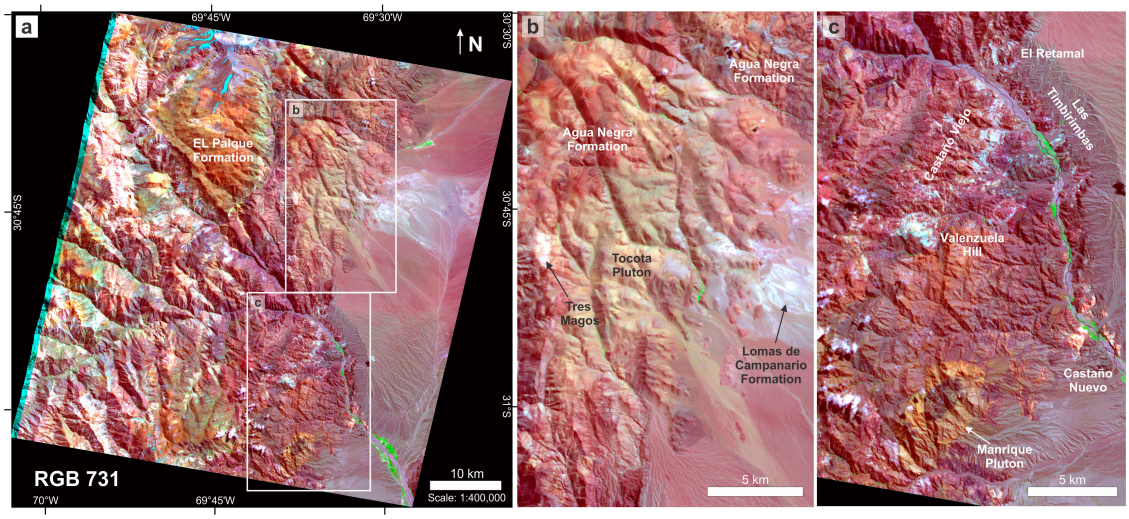

Figure A2. (**a**) False color composite image with ASTER bands 7, 3, 1 (RGB). (**b**) The San Francisco de los Andes district: Tocota pluton (greenish grey), Loma del Campanario (bluish white), Agua Negra Formation (reddish maroon), and Tres Magos alteration zone (white). (**c**) The Castaño area: argillic – phyllic alteration (light blue) and silicic alteration (pink orange), Manrique Pluton and rhyolitic dykes (light brown). Compare the current ASTER imagery with the geologic map in Figure 3.

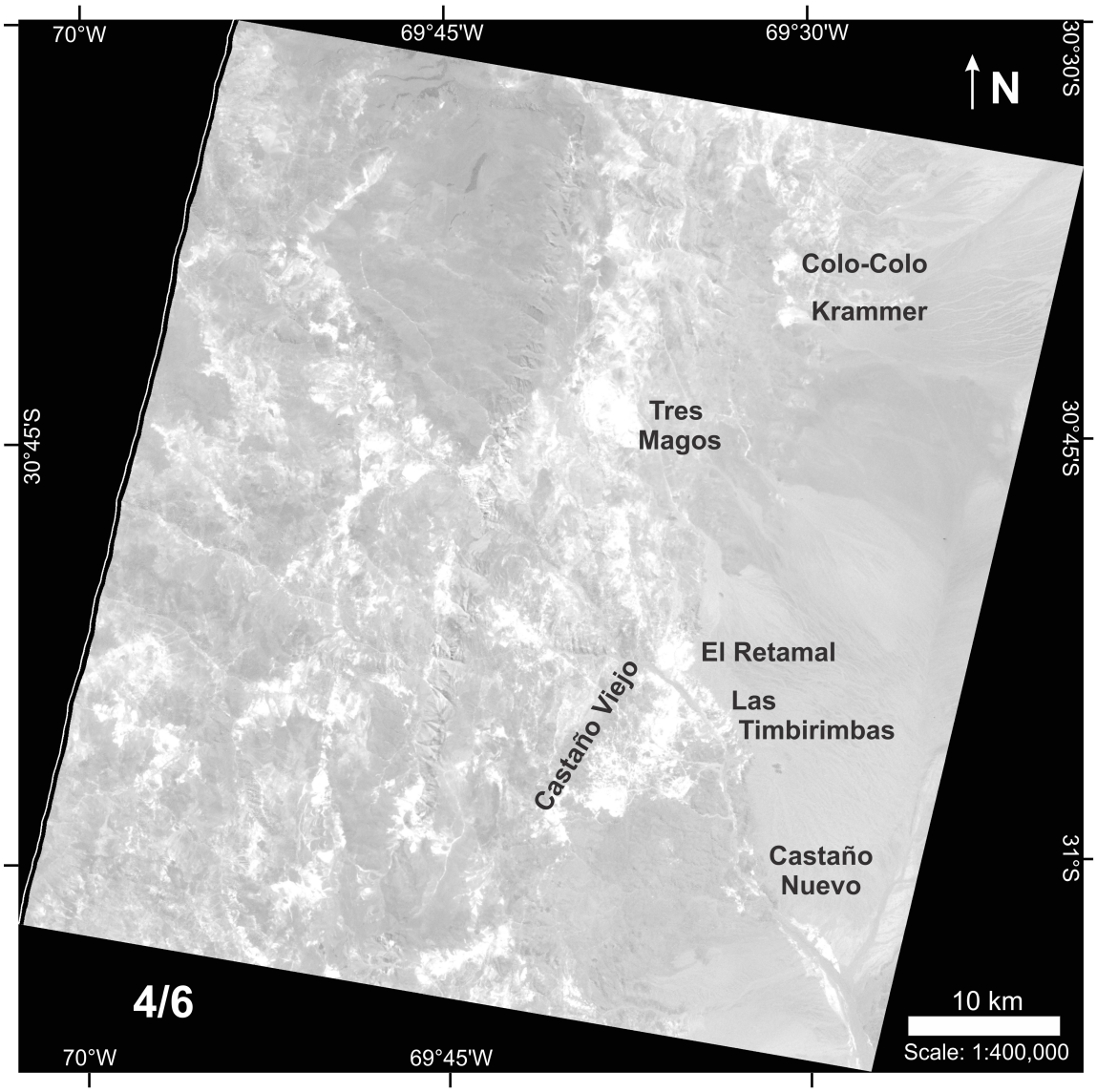

Figure A3. Grey-scale image with the ASTER band ratio 4/6. This band ratio is a good hydrothermal alteration discriminator; it highlights argillic and phyllic alteration in bright colors. It does not provide information regarding lithologic units or areas with silicic alteration.

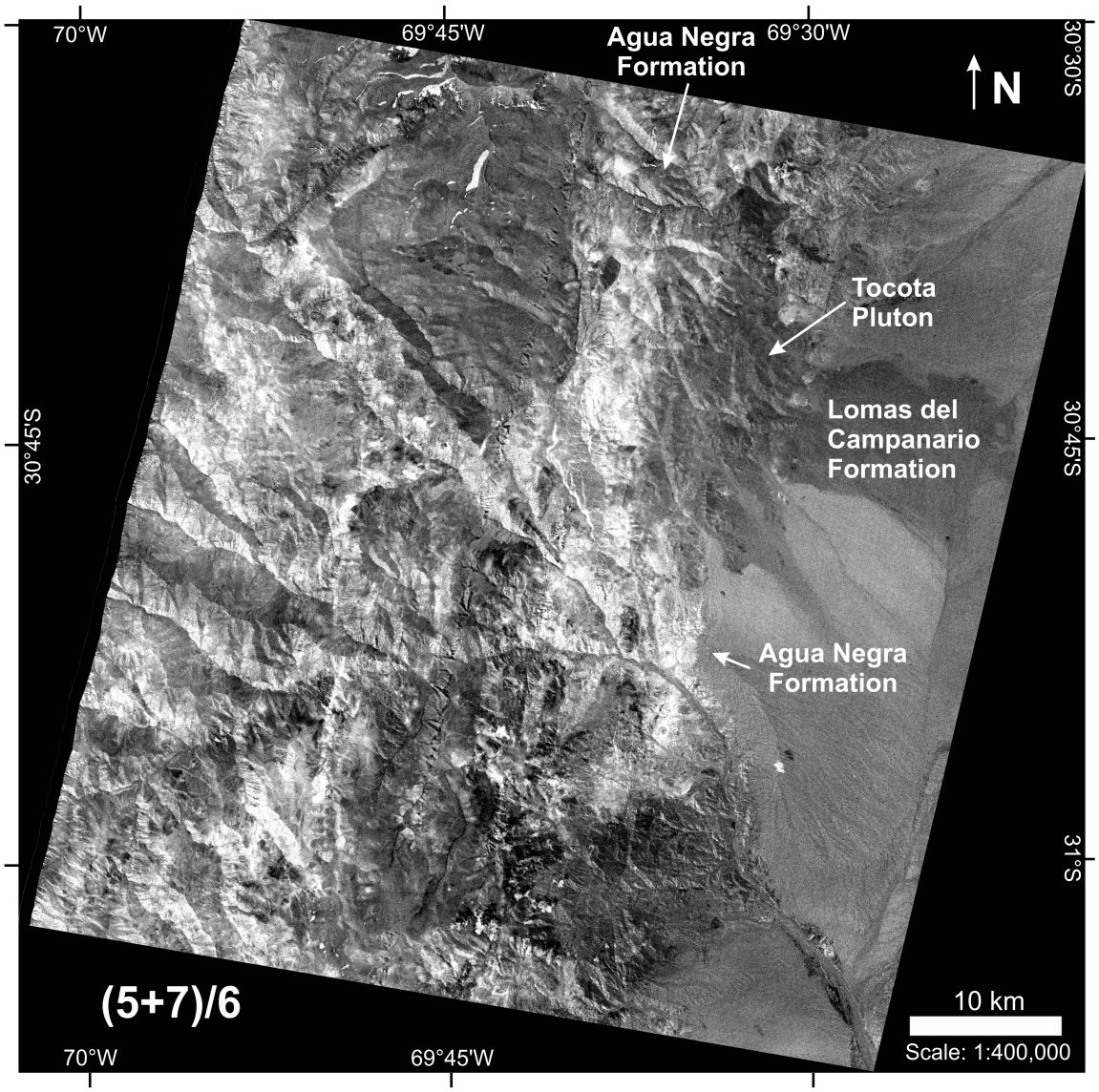

Figure A4. Grey-scale image with the ASTER band operation (5 + 7)/6. The product of this operation differentiates the sedimentary rocks of Agua Negra Formation from the darker Tocota Pluton and El Palque Formation. The Loma del Campanario Formation exhibits darker colors than the alluvial fans.

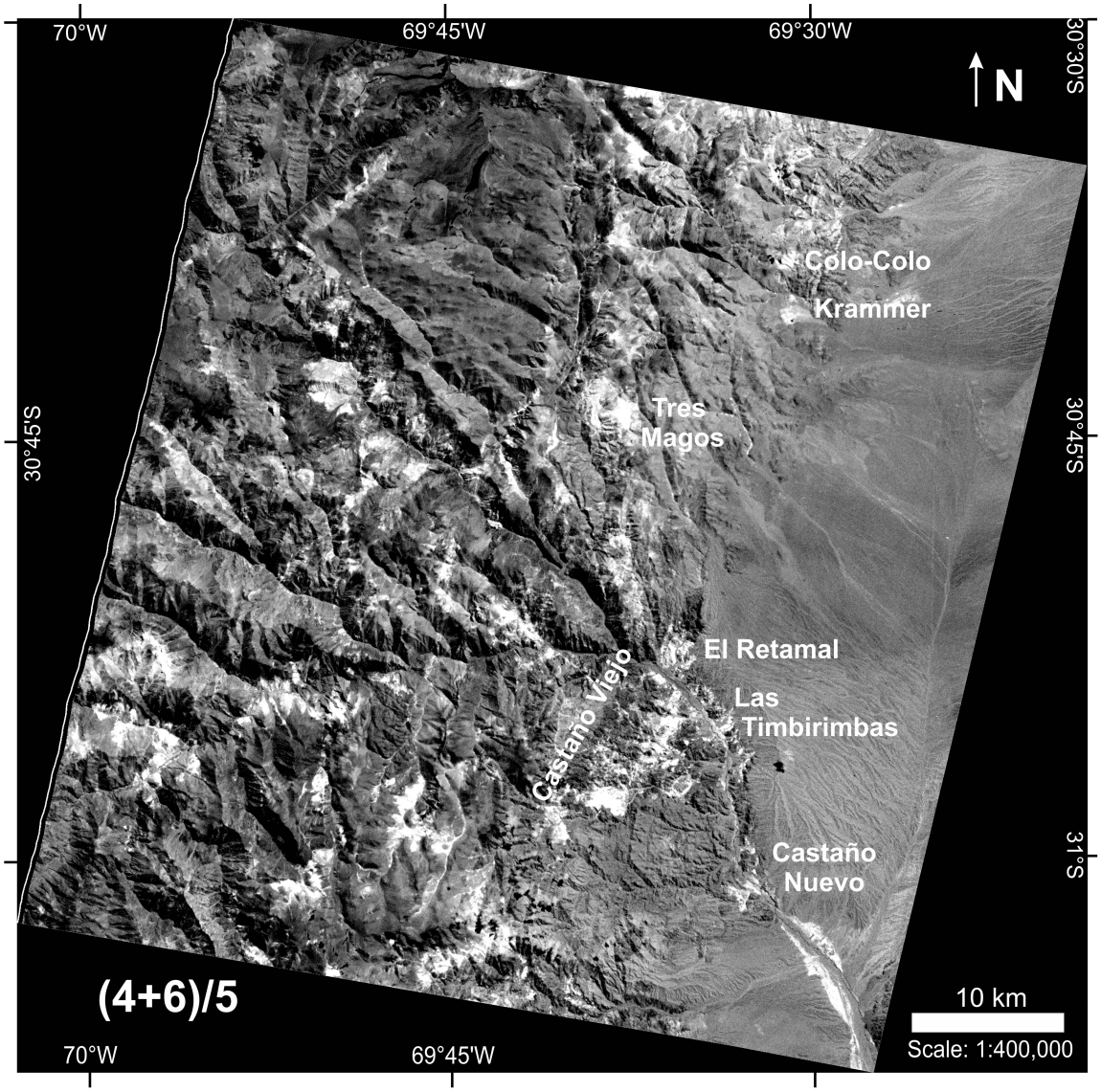

Figure A5. Grey-scale image with the ASTER band operation (4 + 6)/5. This image is particularly useful as it highlights and distinguishes the hydrothermally altered mica-rich and clay-rich areas from the mica-rich sedimentary facies of Agua Negra Formation.

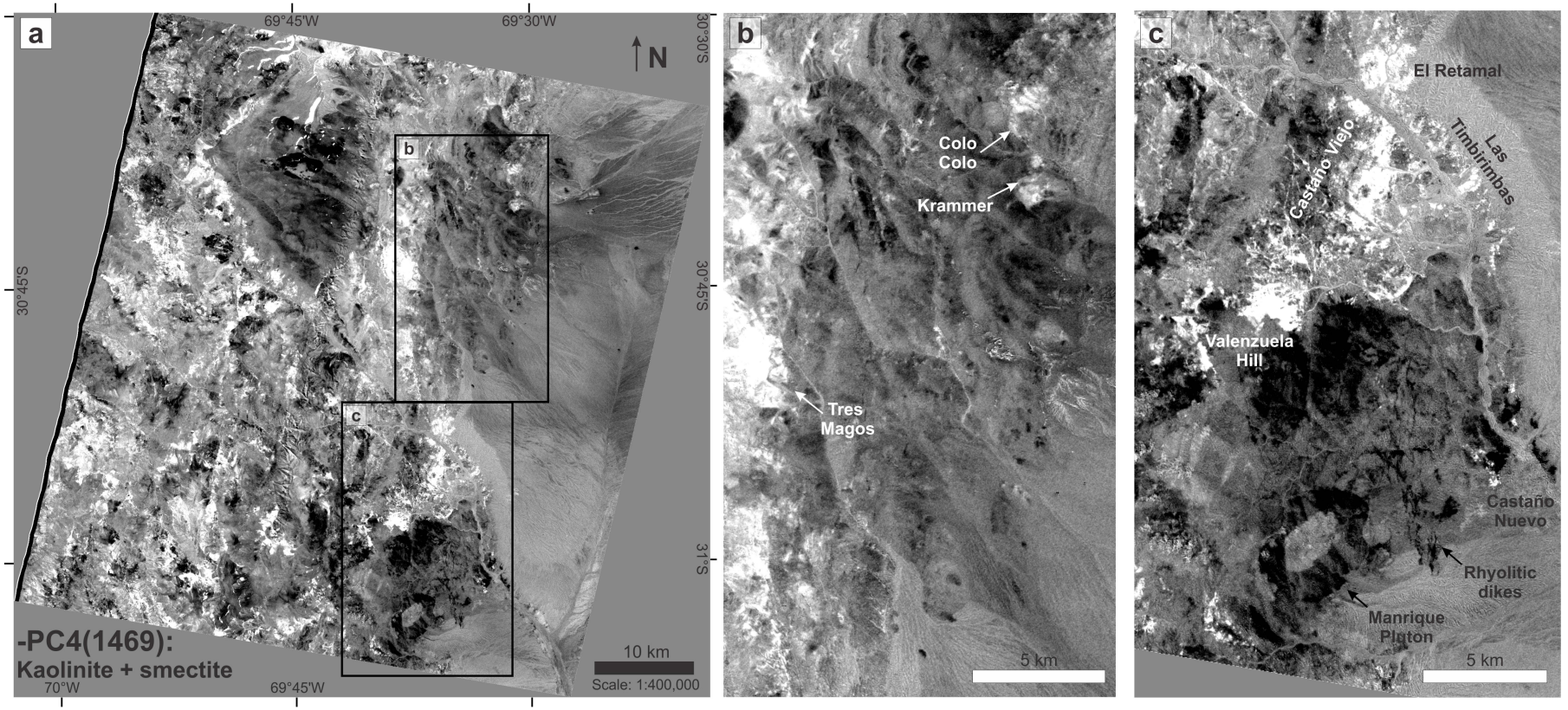

Figure A6. (**a**) Grey-scale image yielded by the negated principal component 4 for bands 1, 4, 6 and 9 (kaolinite and smectite). The white zones represent areas where it is more likely to find kaolinite and smectite (±phyllosilicates). (**b**) In the northern portion of the ASTER scene the hydrothermal alteration associated to Tres Magos, Krammer and Colo-Colo are highlighted. (**c**) In the southern portion of the ASTER scene the hydrothermal alteration associated to the NNE-trending Castaño Viejo alteration zone (from Valenzuela Hill to El Retamal and Las Timbirimbas), and the more restricted Castaño Nuevo alteration zone are detected. The silicic-altered areas at Castaño Nuevo, silica-rich facies at Valenzuela Hill, the Manrique Pluton and rhyolitic dykes are highlighted in black to dark grey.

Table A3. Summary of lithologic units and hydrothermal alteration types detected by the ASTER products presented in this study. This table lists pros and cons, and discuses each processing method applied based on our interpretations and available literature.

ASTER Products	Lithologic Features Detected	Hydrothermal Alteration Features Detected	Additional Comments
Figure A1 – False color composite image: Bands 3 2 1 (RGB)	• Felsic units: El Palque Formation (light brown), Tocota Pluton (orange brown), Loma del Campanario (white), Manrique Pluton and rhyolitic dykes (orange yellow) • Broadly detected sedimentary units: Agua Negra Formation (dark brown)	• Argillic – phyllic alteration (whitish color): Tres Magos, Valenzuela Hill, Castaño Viejo , El Retamal, Las Timbirimbas, and locally Castaño Nuevo • Silicic alteration (whitish color): Castaño Nuevo	• These three ASTER color composite band combinations (RGB) best detected the location of certain geologic units, particularly felsic rocks. They roughly detected hydrothermal alteration zones • The false color composite image 468 is the most comprehensive RGB band combination to detect hydrothermal alteration as it clearly differentiated argillic – phyllic alteration form silicic alteration; It was the only RGB band combination able to highlight Krammer and Colo-Colo argillic hydrothermal alteration zones; and to roughly detect argillic – phyllic alteration zones (pink) affecting the Vega de los Machos Formation (outline surrounding El Palque Formation), and alteration patches to the west of known ore deposits • The three images clearly detected modern alluvial deposits with vegetation and non-hydrothermal clays and/or micas, particularly evident in floodplain adjacent to the Castaño River (e.g., Villanueva village), and more localized areas (e.g., Tocota village and creeks): 321 (bright red), 731 (bright green), 468 (dark brown)
Figure A2 – False color composite image: Bands 7 3 1 (RGB)	• Felsic units: El Palque Formation (orange brown), Tocota Pluton (greenish grey), Loma del Campanario (bluish white), Manrique Pluton and rhyolitic dykes (light brown) • Broadly detected sedimentary units: Agua Negra Formation (reddish maroon)	• Tres Magos argillic alteration zone (white) • Argillic – phyllic alteration (light blue): Valenzuela Hill, Castaño Viejo, El Retamal, Las Timbirimbas, and locally Castaño Nuevo • Silicic alteration (pink orange): Castaño Nuevo	
Figure 5 – False color composite image: Bands 4 6 8 (RGB)	• El Palque Formation (teal), Tocota Pluton (light green), Loma del Campanario (whitish green), Agua Negra Formation (dark green), Manrique Pluton and rhyolitic dykes (greenish blue) • Poor color contrast between units prevent from a clear boundary detection (e.g., Tocota Pluton, Agua Negra and Lomas del Campanario Formation)	• Tres Magos argillic alteration zone (whitish pink) • Argillic – phyllic alteration (pink): Colo-Colo, Krammer, Valenzuela Hill, Castaño Viejo , El Retamal, Las Timbirimbas, and Castaño Nuevo • Silicic alteration (white to light blue): Castaño Nuevo	
Figure 6 – VNIR band ratio: 2/1	• Felsic to intermediate units (light color): El Palque Formation, Puntas Negras Formation, Manrique Pluton and N- trending rhyolitic dykes • Intermediate to mafic units (dark color): Olivares basalts, roof pendant of the Vega de los Machos Formation on top of the Manrique Pluton	**Poor discriminator**: it does not provide major information regarding hydrothermal alteration, only areas with a moderate to strong silicic alteration yielded brighter shades (e.g., Castaño Nuevo and Valenzuela Hill)	**Good lithology** discriminator for igneous rocks based on mineral composition/acidity; particularly useful where lithologic units with contrasting compositions are spatially related or in contact to one another • The 15 m spatial resolution for ASTER bands in the VNIR portion of the electromagnetic spectrum in much higher than SWIR and TIR; thus rhyolitic dykes are best mapped with the 2/1 ratio; In order for these dykes to be detected their width must be larger than the pixel size

Table A3. *Cont.*

ASTER Products	Lithologic Features Detected	Hydrothermal Alteration Features Detected	Additional Comments
Figure A3 – SWIR band ratio: 4/6	**Poor discriminator**: it does not provide information regarding lithology	It highlights argillic and phyllic alteration in white; silicic alteration is undetectable • Argillic – phyllic alteration zones related to known deposits: Colo-Colo, Krammer, Tres Magos, Valenzuela Hill, Castaño Viejo, El Retamal, Las Timbirimbas, and Castaño Nuevo • Argillic – phyllic alteration zones related to barren areas or unknown deposits: Vega de los Machos Formation (white outline surrounding El Palque Formation), and alteration patches to the west of known deposits	**Good hydrothermal alteration discriminator**; it effectively enhanced the response of clay and micas as kaolinite group and OH-bearing minerals have high reflectance in band 4 but low reflectance in band 6, therefore it highlights argillic and phyllic alterations • The ASTER 4/6 SWIR band ratio may lead to wrong interpretations as areas rich in non-hydrothermal clays and/or micas ± vegetation (e.g., sediments from the floodplain adjacent to the Castaño River) are also highlighted
Figure A4 – Math operation: (5+7)/6	• Sandstones and mica-rich siltstones from Agua Negra Formation (light color) • Igneous rocks (dark color): Tocota Pluton, El Palque and Loma del Campanario formations	**Poor discriminator**: it does not provide information regarding hydrothermal alteration	**Good lithology discriminator** to differentiate the sedimentary rocks of Agua Negra Formation from the surrounding igneous rocks; Similarly, the alluvial fans (Rodeo-Calingasta basin) have light grey color that contrasts with the dark-colored igneous rocks (i.e., Tocota Pluton and Loma del Campanario Formation)
Figure A5 – Math operation: (4+6)/5	**Poor discriminator**: it does not provide information regarding lithology	Useful to differentiate hydrothermally altered mica-rich and clay-rich units from unaltered units and the mica-rich sedimentary facies of Agua Negra Formation	**Good hydrothermal alteration discriminator**; it highlighted bright areas that are likely to contain alunite, kaolinite, pyrophyllite and/or illite • Caution is advised as this image may lead to wrong interpretations as areas rich in non-hydrothermal clays and/or micas (e.g., alluvial sediments ± vegetation) are also highlighted
Figure 7 – Math operation: (4x7)/(8x8)	It identifies the location of the Puntas Negras, El Palque, Lomas del Campanario and Las Vizcachas formations in dark shades	• Argillic – phyllic alteration related to known deposits (white): Colo-Colo, Krammer, Tres Magos, Valenzuela Hill, Castaño Viejo , El Retamal, Las Timbirimbas, and Castaño Nuevo • Argillic – phyllic alteration zones related to barren areas or unknown deposits (white): Vega de los Machos Formation (surrounding El Palque Formation), and alteration patches to the west of known deposits • Silicic alteration (black): Castaño Nuevo	**Both good lithology and hydrothermal alteration discriminator within one image**; This operation with a linear enhancement was developed for this study; Both muscovite/illite and kaolinite group minerals have high reflectance in bands 4 and 7, and low reflectance in band 8; The proposed math operation enhanced these spectral features and thus detect phyllic and argillic alteration zones • It broadly highlighted mica- and clay-rich alteration zones and the more local silicified zones in the Castaño Nuevo district; the hydrothermal alteration map for Castaño Nuevo proposed by Troy Resources Ltd helps validate this image efficiency; According to the Troy Ltd website and Delendatti (2003) [20,34], the Castaño Nuevo area has fine grained siliceous alteration located south of the Au–Ag-bearing quartz veins and north of the main argillic – phyllic alteration zone • Pro: Clearly identified the location of Puntas Negras, El Palque, Lomas del Campanario and Las Vizcachas formations • Con: Alluvial deposits rich in non-hydrothermal clays and/or micas ± vegetation were also detected

Table A3. *Cont.*

ASTER Products	Lithologic Features Detected	Hydrothermal Alteration Features Detected	Additional Comments
Figure 8 – False color composite image: Band ratio 4/5 4/6 4/7 (RGB)	• It highlights igneous rocks (maroon): Puntas Negras, El Palque, Lomas del Campanario and Las Vizcachas formations, as well as the Tocota Pluton (purple maroon) • Sedimentary units (light green to light maroon): Agua Negra Formation	• Argillic – phyllic alteration related to known deposits (white to light blue colors): Colo-Colo, Krammer, Tres Magos, Valenzuela Hill, Castaño Viejo , El Retamal, Las Timbirimbas, and Castaño Nuevo • Argillic – phyllic alteration zones related to barren areas or unknown deposits (white to light blue colors): Vega de los Macho Formation (at the base of El Palque rhyolitic flows, which might have affected the underlying unit), and alteration patches to the west of known deposits • Silicic alteration (maroon): Castaño Nuevo	**Good hydrothermal alteration discriminator, which roughly distinguished lithologic units**; It differentiated hydrothermal clays and micas (white light blue) from the mica- and clay-rich facies of Agua Negra Formation (greenish tones); It highlighted well-developed argillic – phyllic alteration zones and local silicic alteration related to known ore deposits • This image may lead to wrong interpretations as areas enriched in non-hydrothermal clays and/or micas ± vegetation (e.g., sediments from the floodplain adjacent to the Castaño River) are also highlighted
Figure 9 – False color composite image: Band ratio 4/5, 4/7 and 3/1 (RGB)	• Acid to intermediate rocks (blue): Manrique and Tocota intrusive bodies and Las Vizcachas, Puntas Negras and El Palque formations • Basic rocks (black to dark green): Olivares Formation • Agua Negra Formation (brown-green and light orange): High contrast between the sedimentary unit and the El Palque Formation and Tocota Pluton (both blue)	• Different argillic – phyllic alteration assemblages related to known deposits based on tonality: 1 - Colo-Colo and Krammer (whitish yellow), 2 - Tres Magos (mustard yellow), 3 - Valenzuela Hill, Castaño Viejo , El Retamal, Las Timbirimbas, and Castaño Nuevo (yellow) • Argillic – phyllic alteration zones related to barren areas or unknown deposits (yellow): Vega de los Machos Formation (surrounding El Palque Formation), and alteration patches to the west of known deposits • It discriminates hydrothermal clays and micas from the non-hydrothermal mica (± clay)-rich sedimentary facies of Agua Negra Formation • Silicic alteration (blue – dark blue): Castaño Nuevo	**Most comprehensive image, it effectively differentiated both lithologic units and types of hydrothermal alteration**; The RGB combination of band ratios 4/5, 4/7 and 3/1 with a linear stretch of 2% contrast was developed for this study; It displayed an enhanced image that provides abundant information within one single image • The band ratios 4/5 and 4/7 were expected to enhance the detection of argillic and phyllic alteration respectively. These ratios are based on kaolinite having high reflectance in band 4 and low reflectance in band 5, whereas muscovite/illite having high reflectance in band 4 and relatively lower reflectance in band 7 • A major advantage is that areas rich in non-hydrothermal clays and/or micas ± vegetation (sediments from the floodplain adjacent to the Castaño River) are detected in white to light blue, not yellow as hydrothermal clays and micas • Bands 1 and 3 have been used traditionally to detect Fe-oxide minerals, but previous studies have documented contrasting spectral responses in felsic and mafic rocks based on these ASTER bands [67]; Basalts have low reflectance in band 1 and higher reflectance in band 3, whereas granites have opposite spectral behavior; The band ratio 3/1 was conceived to aid the detection of granitic plutons and basaltic lavas • The proposed RGB band ratio combination is similar to 4/6, 4/7, 3/1 used by Di Tommaso and Rubinstein (2007) [49], the former gives markedly better results for the study area

Table A3. *Cont.*

ASTER Products	Lithologic Features Detected	Hydrothermal Alteration Features Detected	Additional Comments
Figure 10 – OH-bearing minerals index image (OHIa)	N/A	White pixels represent areas where it is more likely to find phyllosilicates • Alteration zones related to known deposits: Colo-Colo, Krammer, Tres Magos, Valenzuela Hill, Castaño Viejo, El Retamal, Las Timbirimbas, and the more restricted Castaño Nuevo alteration zone • Alteration zones related to barren areas or unknown deposits: Vega de los Machos Formation (surrounding El Palque Formation), alteration patches to the west of known deposits • Agua Negra Formation (light grey pixels between El Palque Formation and the Tocota Pluton) has areas with both phyllosilicate-rich siltstones facies and hydrothermal patches	• The OHIa image is a better and more useful index than OHIb for detecting alteration in the study area; The sericitic alteration zones described by Delendatti (2003) [20] in the Castaño River area are consistently detected by OHIa • Only the lower and intermediate section of Choiyoi Group exhibit an evident mica-rich hydrothermal alteration: (a) The Castaño and Vega de los Machos formations host the ore deposits and hydrothermal alteration associated to Castaño Viejo and Castaño Nuevo; (b) Westward, the Vega de los Machos ± Atutia formations have alteration patches, even though no ore deposit is known to be associated with them • Con: Alluvial deposits rich in non-hydrothermal micas and/or clays ± vegetation were also detected
Figure 11 – Kaolinite index image (KLI)	N/A	White pixels represent areas where it is more likely to find kaolinite • Alteration zones related to known deposits: Idem OHIa (less color contrast) • Alteration zones related to barren areas or unknown deposits: Idem OHIa (less color contrast)	• The KLI image yielded similar responses to OHIa; This behavior is due to kaolinite, which is part of the third group of OH-bearing minerals with absorption features in bands 5 and 6 • Con: Most of the pixels classified as kaolinite are likely to be muscovite or illite, as they have a regional and more abundant distribution, whereas kaolinite is mainly concentrated in the Castaño Nuevo district, as proven by PIMA [20] • Pro: Unlike OHIa, the KLI image did not highlight areas rich in non-hydrothermal clays and/or micas (i.e., primary phyllosilicate-rich siltstones facies of Agua Negra Formation and sediments ± vegetation from the floodplain adjacent to the Castaño River); Only hydrothermal phyllosilicates (± kaolinite) were detected
Figure 12 – Alunite index image (ALI)	N/A	White pixels represent areas where it is more likely to find alunite • Alteration zones related to known deposits: Krammer, Tres Magos, and Valenzuela Hill	ALI's strong responses at Valenzuela Hill, Tres Magos and Krammer are supported by field verification at Valenzuela Hill and extrapolated to Tres Magos and Krammer due to similar pixel information; Diffuse and isolated white pixels elsewhere in the Castaño Viejo region, Castaño Nuevo and Las Timbirimbas can potentially relate to trace contents of alunite (with clays and phyllosilicate admixtures); At El Retamal, the spectral response to the ALI was very poor • Con: Washed-out image; Except for the white pixels related to alunite, the overall image exhibits light grey shades with very low contrast

Table A3. *Cont.*

ASTER Products	Lithologic Features Detected	Hydrothermal Alteration Features Detected	Additional Comments
Figure 13 – Quartz index image (QI)	• It is particularly usefully for detailed mapping of the limits of the Tocota Pluton and Lomas del Campanario Formation (dark color) • Sedimentary units including Agua Negra Formation and the alluvial fans (Rodeo-Calingasta basin) have white color • Based on color contrast, QI effectively discriminates the Tocota Pluton from the Agua Negra Formation	N/A	• It effectively discriminated the Tocota Pluton from the Agua Negra sedimentary rocks, with sharply defined limits: The Tocota Pluton contains abundant quartz and alkali feldspar, thus the dark grey shades; The sedimentary facies of Agua Negra Formation contain little or no alkali feldspar, resulting in very bright areas • The western, northern and southern limit of the Tocota Pluton are abrupt, making this index a very effective mapping tool. The contacts between the Tocota Pluton and Agua Negra Formation are undetected or less evident in other satellite images and aerial photos, and are merely simplified boundaries in geologic maps • The north-eastern and south-eastern limit of the Tocota Pluton is covered by thick unconsolidated Quaternary gravel deposits accumulated at the base of the Andes; The gravels are rich in quartz but poor in alkali feldspar, resulting in a light color contrasting with the dark pixels of the Tocota Pluton • The eastern limit of the pluton is covered by the Lomas del Campanario andesite to dacite ignimbrites and tuffs: These volcaniclastic rocks have a similar shade of grey to the Tocota Pluton making these units difficult to discriminate based on tonality; Conversely, the intrusive body has a rough texture, whereas the volcanic unit has a smoother texture, which assists in distinguishing both units
Figure 14 – Negated principal component 4 for bands 1, 4, 6 and 7 (kaolinite)	N/A	White pixels represent areas more likely to contain kaolinite • Alteration zones related to known deposits: Colo-Colo, Krammer, Tres Magos, Valenzuela Hill, Castaño Viejo, El Retamal, Las Timbirimbas, and the more restricted Castaño Nuevo alteration zone • Alteration zones related to barren areas or unknown deposits: Vega de los Machos Formation (white outline surrounding El Palque Formation), and alteration patches to the west of known deposits	• Based on our interpretations of band operations and Ninomiya's indices coupled with previous field studies, bright pixels are inferred to highlight areas rich in OH-bearing minerals, not only kaolinite • The dark areas in Castaño Viejo are interpreted to represent strongly silicic-altered rocks; Similarly, the dark regions near Valenzuela Hill could be areas enriched in secondary quartz, or simply silica-rich facies in the andesitic porphyry [20] • Con: Alluvial deposits rich in non-hydrothermal micas and/or clays were also detected
Figure A6 – Negated principal component 4 for bands 1, 4, 6 and 9 (kaolinite and smectite)	N/A	White pixels represent areas more likely to contain kaolinite and smectite • Alteration zones related to known deposits: Idem –PC4 (1467), better contrast • Alteration zones related to barren areas or unknown deposits: Idem –PC4 (1467), better contrast	• It shows similar areas as the negated PC4 for bands 1467 • As discussed above, there are many areas with bright pixels where illite is present instead of kaolinite or smectite • The silicic-altered areas in Castaño Viejo and the silica-rich facies in Valenzuela Hill are more evident with this PC; Felsic units such as the Manrique Pluton or the N-trending rhyolitic dykes are highlighted in dark grey tones in both Figures 14 and A6 • Alluvial deposits are less evident in this PCA image

Table A3. *Cont.*

ASTER Products	Lithologic Features Detected	Hydrothermal Alteration Features Detected	Additional Comments
Figure 15 – Principal component 3 for bands 1, 3, 5 and 7 (alunite)	N/A	White pixels represent areas more likely to contain alunite • Alteration zones related to known deposits: Tres Magos, and Valenzuela Hill	• It shows consistent areas with ALI; This image has markedly less 'noise' (bright pixels unrelated to alunite), and is less washed out than ALI • Cluster of white pixels located close to Valenzuela Hill and close to the Tres Magos mine (unlike ALI, the alteration at Krammer is undetected) • The large NNE-trending hydrothermal alteration in the Castaño Viejo district is no longer evident, only scarce white pixels at Castaño Viejo, El Retamal and Las Timbirimbas; Similarly, the alteration zones at Krammer and Colo-Colo are not highlighted due to alunite absence • Valenzuela Hill is the only control area where alunite is abundant and detected by PIMA [20]. No PIMA/TerraSpec data is available for the Tres Magos area, but based on similar pixel information (and consistency with ALI) the presence of alunite may be inferred

References

1. Hunt, G.R. Spectral signatures of particulate minerals in the visible and near infrared. *Geophysics* **1977**, *42*, 501–513. [CrossRef]
2. Hunt, G.R.; Ashley, R.P. Spectra of altered rocks in the visible and near infrared. *Econ. Geol.* **1979**, *74*, 1613–1629. [CrossRef]
3. Crowley, J.K.; Vergo, N. Near-infrared reflectance spectra of mixtures of kaolin-goup minerals: Use in clay mineral studies. *Clays Clay Miner.* **1988**, *36*, 310–316. [CrossRef]
4. Clark, R.N.; King, T.V.V.; Klejwa, M.; Swayze, G.A.; Vergo, N. High spectral resolution reflectance spectroscopy of minerals. *J. Geophys. Res.* **1990**, *95*, 12653–12680. [CrossRef]
5. Hunt, G.R.; Salisbury, J.W. *Mid-Infrared Spectral Behavior of Igneous Rocks*; Technical Report AFRCL-TR-75-0356; Air Force Cambridge Research Laboratories: Cambridge, MA, USA, 1974.
6. Markham, B.; Storey, J.; Morfitt, R. Landsat-8 sensor characterization and calibration. *Remote Sens.* **2015**, *7*, 2279–2282. [CrossRef]
7. Loughlin, W.P. Principal component analysis for alteration mapping. *Photogramm. Eng. Remote Sens.* **1991**, *57*, 1163–1169.
8. Nielsen, R.L.; Mancuso, J.D.; Miller, R.A.; Sabins, F.F., Jr. *Use of Thematic Mapping Imagery in Generative Mineral Exploration, Central Andes of South America*; Preprint Number 95-9; Society for Mining, Metallurgy and Exploration Inc.: Englewood, CO, USA, 1995; pp. 1–5.
9. Knight, E.J.; Kvaran, G. Landsat-8 operational land imager design, characterization and performance. *Remote Sens.* **2014**, *6*, 10286–10305. [CrossRef]
10. Kaab, A.; Huggel, C.; Paul, F.; Wessels, R.; Raup, B.; Kieffer, H.; Kargel, J. Glacier monitoring from ASTER imagery: Accuracy and applications. In Proceedings of the EARSeL-LISSIG-Workshop Observing our Cryosphere from Space, Bern, Switzerland, 11–13 March 2002; pp. 43–53.
11. Barsi, J.A.; Schott, J.R.; Hook, S.J.; Raqueno, N.G.; Markham, B.L.; Radocinski, R.G. Landsat-8 thermal infrared sensor (TIRS) vicarious radiometric calibration. *Remote Sens.* **2014**, *6*, 11607–11626. [CrossRef]
12. Irons, J.R.; Taylor, M.P.; Rocchio, L. Landsat Science—Landsat 8. Available online: https://landsat.gsfc.nasa.gov/landsat-data-continuity-mission/ (accessed on 20 November 2017).
13. Barsi, J.A.; Lee, K.; Kvaran, G.; Markham, B.L.; Pedelty, J.A. The spectral response of the Landsat-8 operational land imager. *Remote Sens.* **2014**, *6*, 10232–10251. [CrossRef]
14. Abrams, M.; Hook, S.J. Simulated ASTER data for geologic studies. *IEEE Trans. Geosci. Remote Sens.* **1995**, *33*, 692–699. [CrossRef]
15. Fujisada, H. Design and performance of ASTER instrument. *Proc. SPIE* **1995**, 16–25.
16. Yamaguchi, Y.; Fujisada, H.; Kudoh, M.; Kawakami, T.; Tsu, H.; Kahle, A.B.; Pniel, M. ASTER instrument characterization and operation scenario. *Adv. Space Res.* **1999**, *23*, 1415–1424. [CrossRef]
17. Abrams, M. The Advanced Spaceborne Thermal Emission and Reflection Radiometer (ASTER): Data products for the high spatial resolution imager on NASA's Terra platform. *Int. J. Remote Sens.* **2000**, *21*, 847–859. [CrossRef]
18. Yamaguchi, Y.I.; Fujisada, H.; Kahle, A.B.; Tsu, H.; Kato, M.; Watanabe, H.; Sato, I.; Kudoh, M. ASTER instrument performance, operation status and application to Earth sciences. In Proceedings of the IEEE International Geosciences and Remote Sensing Symposium, Sydney, Australia, 9–13 July 2001; Volume 3, pp. 1215–1216.
19. Abrams, M.; Hook, S.; Ramachandran, B. *ASTER User Handbook*; Version 2; Jet Propulsion Laboratory and EROS Data Center, NASA: Sioux Falls, SD, USA, 2002.
20. Delendatti, G.L. Caracterización de zonas de alteración hidrotermal en las márgenes del río Castaño, provincia de San Juan, mediante procesamiento digital de imágenes TM. *Revista de la Asociación Geológica Argentina* **2003**, *58*, 97–108.
21. Testa, F.J. Geology, Alteration, Mineralization and Geochemistry of Tourmaline Breccia Complexes in the Andes: Rio Blanco-Los Bronces, Chile and San Francisco de los Andes, Argentina. Ph.D. Thesis, University of Tasmania, Hobart, Australia, 2017.
22. Ninomiya, Y. A Stabilized Vegetation Index and Several Mineralogic Indices Defined for ASTER VNIR and SWIR Data. In Proceedings of the IEEE International Geoscience and Remote Sensing Symposium, Toulouse, France, 21–25 July 2003; Volume 3, pp. 1552–1554.
23. Ninomiya, Y. Lithologic mapping with multispectral ASTER TIR and SWIR data. *Proc. SPIE* **2004**, *5234*, 180–190.

24. Ninomiya, Y.; Fu, B. Quartz index, carbonate index and SiO_2 content index defined for ASTER TIR data. *J. Remote Sens. Soc. Jpn.* **2002**, *22*, 50–61.
25. Crósta, A.P.; De Souza Filho, C.R.; Azevedo, F.; Brodie, C. Targeting key alteration minerals in epithermal deposits in Patagonia, Argentina, using ASTER imagery and principal component analysis. *Int. J. Remote Sens.* **2003**, *24*, 4233–4240. [CrossRef]
26. Rodríguez Fernández, L.R.; Heredia, N.; Gallastegui, G.; Quesada, C.; Robador, A.; Marín, G.; Cardó, D.R. *Texto Explicativo de la Carta Geológica No 3169-14 a Escala 1:100.000 (Paraje de Castaño Viejo)*; Instituto de Geología y Recursos Minerales, Servicio Geológico Minero Argentino (SEGEMAR): Buenos Aires, Argentina, 1996; p. 145.
27. Rodríguez Fernández, L.R.; Heredia, N.; Marín, G.; Quesada, C.; Robador, A.; Ragona, D.; Cardó, R. Tectonoestratigrafia y estructura de los Andes Argentinos entre los 30°30′y 31°00′ de latitud Sur. In Proceedings of the XIII Congreso Geológico Argentino y III Congreso de Exploración de Hidrocarburos, Buenos Aires, Argentina, 13–18 October 1996; Volume II, pp. 111–124.
28. Espina, R.G.; Cegarra, M.; Ragona, D.; Gonzalez, P.D.; Lo Forte, G.L.; Escuer, J.; Arias, D. *Descripción Geológica de la Hoja "Paraje Castaño Nuevo", No 3169-20, Provincia de San Juan. Escala 1:100.000*; Secretaría de Minería de la Nación: Buenos Aires, Argentina, 1998; p. 85.
29. Cegarra, M.I.; Ragona, D.; García Espina, R.; González, P.D.; Lo Forte, G.L.; Sato, A.M. Estratigrafía de la región de Castaño Nuevo, Cordillera Frontal de San Juan. In Proceedings of the 10° Congreso Latinoamericano de Geología y 6° Congreso Nacional de Geología Económica, Buenos Aires, Argentina, 8–13 Novermber 1998; Volume 1, pp. 85–90.
30. Heredia, N.; Rodríguez Fernández, L.R.; Gallastegui, G.; Busquets, P.; Colombo, F. Geological setting of the Argentine Frontal Cordillera in the flat-slab segment (30°00′–31°30′S latitude). *J. S. Am. Earth Sci.* **2002**, *15*, 79–99. [CrossRef]
31. Rodríguez Fernández, L.R.; Heredia, N.; Espina, R.G.; Cegarra, M.I. Estratigrafía y estructura de los Andes Centrales Argentinos entre los 30° y 31° de Latitud Sur. Stratigraphy and Structure of the Argentine Central Andes between 30° and 31° S latitude. *Acta Geológica Hispánica* **1999**, *32*, 51–75.
32. Cardó, R.; Díaz, I.N. *Descripción de la Hoja Geológica 3169-1 Rodeo, Provincia de San Juan. Escala 1:250.000*; Instituto de Geología y Recursos Minerales, Servicio Geológico Minero Argentino (SEGEMAR): Buenos Aires, Argentina, 2005; p. 47.
33. Cardó, R. Distrito polimetálico Castaño Viejo, San Juan. In *Recursos Minerales de la República Argentina*; Zappettini, E.O., Ed.; Instituto de Geología y Recursos Minerales, SEGEMAR: Buenos Aires, Argentina, 1999; pp. 857–863.
34. Troy Resources Limited—Castaño Nuevo Project. Available online: http://www.troyres.com.au/ (accessed on 2 August 2014).
35. Hedenquist, J.W. *Research Applied to Mineral Exploration: Observations on Epithermal Mineralization in the Casposo and Castaño Nuevo Districts, San Juan, Argentina*; Hedenquist Consulting, Inc.: Ottawa, ON, Canada, 2012; pp. 1–28.
36. Angelelli, V. *Yacimientos Metaliferos de la Republica Argentina*; Comisión de Investigaciones Científicas de la Provincia de Buenos Aires, Facultad de Ciencias Naturales y Museo de La Plata—UNLP, Instituto de Geologia Aplicada: La Plata, Argentina, 1984; pp. 1–704.
37. Testa, F.; Cooke, D.; Zhang, L.; Mas, G. Bismoclite (BiOCl) in the San Francisco de los Andes Bi–Cu–Au Deposit, Argentina. First Occurrence of a Bismuth Oxychloride in a Magmatic–Hydrothermal Breccia Pipe and Its Usefulness as an Indicator Phase in Mineral Exploration. *Minerals* **2016**, *6*, 62. [CrossRef]
38. Cardó, R.; Segal, S.; Korzeniewski, L.I.; Palacio, M.B.; Chernicoff, C. Estudio Metalogenético de brechas hidrotermales portadoras de mineralización de Bi–Au–Cu en el ámbito de Cordillera Frontal, provincia de San Juan. In *Serie Contribuciones Técnicas, Recursos Minerales N° 31*; Servicio Geologico Minero Argentino, SEGEMAR: Buenos Aires, Argentina, 2008; pp. 2–28.
39. Wetten, A.F. Distrito Minero Tocota, San Juan. In *Recursos Minerales de la República Argentina*; Zappettini, E.O., Ed.; Instituto de Geología y Recursos Minerales, SEGEMAR: Buenos Aires, Argentina, 1999; pp. 821–827.
40. Machuca, E.; Grassi, I.; Cruz, P.; Rodríguez, J.; Atencio, M.; Ledesma, M. Evidencias de un pórfido mineralizado en el area de Tocota, departamento Iglesia, San Juan, Argentina. In Proceedings of the 7° Congreso Geológico Chileno, Concepcion, Chile, 17–21 October 1994; Volume II, pp. 843–847.

41. Delendatti, G.L.; Bastías, H. Características de la alteración hidrotermal en el distrito El Retamal, San Juan, y su relación con zonas anómalas en Au–Cu. In Proceedings of the VII Congreso Argentino de Geología Económica, Salta, Argentina, 26–28 September 2001; Volume 1, pp. 73–76.
42. Exelis Visual Information Solutions (ENVI). *Atmospheric Correction Module: QUAC and FLAASH User's Guide*; Exelis Visual Information Solutions: Porter, CO, USA, 2009.
43. Adler-Golden, S.; Berk, A.; Bernstein, L.S.; Richtsmeier, S.; Acharya, P.; Matthew, M.W.; Anderson, G.P.; Allred, C.L.; Jeong, L.S.; Chetwynd, J. Flaash, a modtran4 atmospheric correction package. In *AVIRIS Workshop Proceedings*; NASA Jet Propulsion Laboratory, California Institute of Technology: La Cañada Flintridge, CA, USA, 1998; Volume 4.
44. Rani, N.; Mandla, V.R.; Singh, T. Evaluation of atmospheric corrections on hyperspectral data with special reference to mineral mapping. *Geosci. Front.* **2017**, *8*, 797–808. [CrossRef]
45. Chang, Z.; Yang, Z. Scientific Communications: Evaluation of Inter-Instrument Variations among Short Wavelength Infrared (SWIR) Devices. *Econ. Geol.* **2012**, *107*, 1479–1488. [CrossRef]
46. Baldridge, A.M.; Hook, S.J.; Grove, C.I.; Rivera, G. The ASTER spectral library version 2.0. *Remote Sens. Environ.* **2009**, *113*, 711–715. [CrossRef]
47. Mars, J.C.; Rowan, L.C. Regional mapping of phyllic- and argillic-altered rocks in the Zagros magmatic arc, Iran, using Advanced Spaceborne Thermal Emission and Reflection Radiometer (ASTER) data and logical operator algorithms. *Geosphere* **2006**, *2*, 161–186. [CrossRef]
48. Pour, A.B.; Hashim, M. The application of ASTER remote sensing data to porphyry copper and epithermal gold deposits. *Ore Geol. Rev.* **2012**, *44*, 1–9. [CrossRef]
49. Di Tommaso, I.; Rubinstein, N. Hydrothermal alteration mapping using ASTER data in the Infiernillo porphyry deposit, Argentina. *Ore Geol. Rev.* **2007**, *32*, 275–290. [CrossRef]
50. Hunt, G.R.; Salisbury, J.W. Visible and near infrared spectra of minerals and rocks: II. Carbonates. *Mod. Geol.* **1971**, *2*, 23–30.
51. Hunt, G.R. Near-infrared (1.3–2.4) μm spectra of alteration minerals—Potential for use in remote sensing. *Geophysics* **1979**, *44*, 1974–1986. [CrossRef]
52. Spatz, D.M.; Wilson, R.T. Remote sensing characteristics of porphyry copper systems, western America Cordillera. In *Porphyry Copper Deposits of the American Cordillera*; Pierce, F.W., Bolm, J.G., Eds.; Arizona Geological Society Digest: Tucson, AZ, USA, 1995; pp. 94–108.
53. Dalton, J.B.; Bove, D.J.; Mladinich, C.S.; Rockwell, B.W. Identification of spectrally similar materials using the USGS Tetracorder algorithm: The calcite–epidote–chlorite problem. *Remote Sens. Environ.* **2004**, *89*, 455–466. [CrossRef]
54. Rowan, L.C.; Schmidt, R.G.; Mars, J.C. Distribution of hydrothermally altered rocks in the Reko Diq, Pakistan mineralized area based on spectral analysis of ASTER data. *Remote Sens. Environ.* **2006**, *104*, 74–87. [CrossRef]
55. Boloki, M.; Poormirzaee, R. Using ASTER Image Processing for Hydrothermal Alteration and Key Alteration Minerals Mapping in Siyahrud area, IRAN. *Int. J. Geol.* **2009**, *3*, 38–43.
56. Alimohammadi, M.; Alirezaei, S.; Kontak, D.J. Application of ASTER data for exploration of porphyry copper deposits: A case study of Daraloo-Sarmeshk area, southern part of the Kerman copper belt, Iran. *Ore Geol. Rev.* **2015**, *70*, 290–304. [CrossRef]
57. Feizi, F.; Mansuri, E. Identification of Alteration Zones with Using ASTER Data in A Part of Qom Province, Central Iran. *J. Basic Appl. Sci. Res.* **2012**, *2*, 10173–10184.
58. Rowan, L.C.; Mars, J.C. Lithologic mapping in the Mountain Pass, California area using Advanced Spaceborne Thermal Emission and Reflection Radiometer (ASTER) data. *Remote Sens. Environ.* **2003**, *84*, 350–366. [CrossRef]
59. Rowan, L.C.; Mars, J.C.; Simpson, C.J. Lithologic mapping of the Mordor, NT, Australia ultramafic complex by using the Advanced Spaceborne Thermal Emission and Reflection Radiometer (ASTER). *Remote Sens. Environ.* **2005**, *99*, 105–126. [CrossRef]
60. Van der Meer, F.D.; van der Werff, H.M.A.; van Ruitenbeek, F.J.A.; Hecker, C.A.; Bakker, W.H.; Noomen, M.F.; van der Meijde, M.; Carranza, E.J.M.; De Smeth, J.B.; Woldai, T. Multi- and hyperspectral geologic remote sensing: A review. *Int. J. Appl. Earth Obs. Geoinf.* **2012**, *14*, 112–128. [CrossRef]
61. Van der Meer, F.D.; van der Werff, H.M.A.; van Ruitenbeek, F.J.A. Potential of ESA's Sentinel-2 for geological applications. *Remote Sens. Environ.* **2014**, *148*, 124–133. [CrossRef]
62. Hewson, R. Summary of the 22nd ASTER Science Meeting, Tokyo, Japan, 20–23 May 2002. Available online: http://www.eoc.csiro.au/reports/hewson/22aster.htm (accessed on 29 January 2018).

63. Marquetti, C.; Becchio, R.; Seggiaro, R.; Nakashima, K. Aplicacion de datos ASTER para el mapeo de la hoja geológica Andalgalá, Catamarca, Argentina. In Proceedings of the 1° Simposio ASTER–GEOSAT, Buenos Aires, Argentina, 4–5 November 2004.
64. Amer, R.; Kusky, T.; Ghulam, A. Lithological mapping in the Central Eastern Desert of Egypt using ASTER data. *J. Afr. Earth Sci.* **2010**, *56*, 75–82. [CrossRef]
65. Pazand, K.; Sarvestani, J.F.; Ravasan, M.R.S. Hydrothermal Alteration Mapping Using ASTER Data for Reconnaissance Porphyry Copper Mineralization in the Ahar Area, NW Iran. *J. Indian Soc. Remote Sens.* **2013**, *41*, 379–389. [CrossRef]
66. Pérez, D.J.; Azcurra, D.; D'Odorico, P.; Sequeira, N. Mapeo de alteración hidrotermal con datos ASTER, en la región de La Coipa, Cordillera Frontal (31°45'S), Provincia de San Juan, Argentina. In Proceedings of the Anais XIII Simpósio Brasileiro de Sensoriamento Remoto, Florianópolis, Brazil, 21–26 April 2007; pp. 2095–2102.
67. Masoumi, F.; Eslamkish, T.; Abkar, A.A.; Honarmand, M.; Harris, J.R. Integration of spectral, thermal and textural features of ASTER data using Random Forests classification for lithological mapping. *J. Afr. Earth Sci.* **2017**, *129*, 445–457. [CrossRef]
68. Zhang, X.; Pazner, M. Comparison of Lithologic Mapping with ASTER, Hyperion and ETM Data in the Southeastern Chocolate Mountains, USA. *Photogramm. Eng. Remote Sens.* **2007**, *73*, 555–561. [CrossRef]
69. Ninomiya, Y. Advanced Remote Lithologic Mapping in Ophiolite Zone with ASTER Multispectral Thermal Infrared Data. In Proceedings of the IEEE International Geoscience and Remote Sensing Symposium, Toulouse, France, 21–25 July 2003; Volume 3, pp. 1561–1563.
70. Ninomiya, Y.; Fu, B.; Cudahy, T.J. Detecting lithology with Advanced Spaceborne Thermal Emission and Reflection Radiometer (ASTER) multispectral thermal infrared "radiance-at-sensor" data. *Remote Sens. Environ.* **2005**, *99*, 127–139. [CrossRef]
71. Rockwell, B.W.; Hofstra, A.H. Identification of quartz and carbonate minerals across northern Nevada using ASTER thermal infrared emissivity data—Implications for geologic mapping and mineral resource investigations in well-studied and frontier areas. *Geosphere* **2008**, *4*, 218–246. [CrossRef]
72. Guha, A.; Kumar, K.V. New ASTER derived thermal indices to delineate mineralogy of different granitoids of an Archaean Craton and analysis of their potentials with reference to Ninomiya's indices for delineating quartz and mafic minerals of granitoids—An analysis in Dharwar Cr. *Ore Geol. Rev.* **2016**, *74*, 76–87. [CrossRef]
73. Ninomiya, Y. Quantitative estimation of SiO_2 content in igneous rocks using thermal infrared spectra with a neural network approach. *IEEE Trans. Geosci. Remote Sens.* **1995**, *33*, 684–691. [CrossRef]
74. Pearson, K. On lines and planes of closest fit to systems of points in space. *Philos. Mag.* **1901**, *2*, 559–572. [CrossRef]
75. Hotelling, H. Analysis of a complex of statistical variables into principal components. *J. Educ. Psychol.* **1933**, *24*, 417–441. [CrossRef]
76. Crosta, A.P.; Moore, J.M. Enhancement of Landsat Thematic Mapper imagery for residual soil mapping in SW Minas Gerais State Brazil: A prospecting case history in greenstone belt terrain. In Proceedings of the 9th Thematic Conference on Remote Sensing for Exploration Geology, Calgary, AB, Canada, 2–6 October 1989; pp. 1173–1187.
77. Crósta, A.P.; Prado, I.D.M.; Obara, M. The use of Geoscan AMSS Mk-II data for gold exploration in the Rio Itapicuru greenstone belt, Bahia, Brazil. In Proceedings of the 11th Thematic Conference on Remote Sensing for Exploration Geology, Las Vegas, NV, USA, 27–29 February 1996; pp. 205–214.
78. Prado, I.D.M.; Crósta, A.P. Evaluating Geoscan AMSS Mk-II for gold exploration in the Fazenda Maria Preta District, Rio Itapicuru greenstone belt, Bahia State, Brazil. *Bol. IG-USP* **1997**, *28*, 63–84. [CrossRef]
79. Xu, Y.; Lin, Q.; Shao, Y.; Wang, L. Extraction Mechanism of Alteration Zones using ASTER Imagery. In Proceedings of the IEEE International Geosciences and Remote Sensing Symposium, Anchorage, AK, USA, 20–24 September 2004; Volume 6, pp. 4174–4175.
80. Bierwirth, P.N. Laboratory and imaging spectroscopy of tourmaline—A tool for mineral exploration. In Proceedings of the 14th Australasian Remote Sensing and Photogrammetry Conference, Darwin, Australia, 29 September–3 October 2008.